J. Fluid Mech. (2014), *vol.* 757, *pp.* 179–207.
doi:10.1017/jfm.2014.483

The boundary layer instability of a gliding fish helps rather than prevents object identification

Audrey P. Maertens[1,†] **and Michael S. Triantafyllou**[1]

[1]Center for Ocean Engineering, Massachusetts Institute of Technology, 77 Massachusetts Avenue, Cambridge, MA 02139, USA

(Received 28 April 2014; revised 22 July 2014; accepted 17 August 2014; first published online 19 September 2014)

Inspired by the function of the lateral line in aquatic animals, we study the shape identification of a stationary cylinder through pressure measurements made by sensors located on the surface of a steadily moving foil, modelling a fish gliding in close proximity to an object. Comparing experimental results, potential flow predictions and viscous simulations, we first show that the pressure in the boundary layer of the foil is significantly affected by unsteady viscous effects, especially in the posterior half of the foil. Therefore, even after the effects of the boundary layer thickness are accounted for, potential flow predictions are inaccurate. Subsequently, we show that the spatial features of the unsteady patterns developing when the foil is moving near a cylinder can be predicted accurately through linear stability analysis of the average boundary layer velocity profile under open water conditions. Because these unsteady patterns result from amplification of the potential flow-like disturbance caused in the front part of the foil, they are specific to the cylinder that generated them and could be used to identify its shape. We develop and demonstrate a methodology to calculate the unsteady pressure based on combining potential flow predictions with results from linear stability analysis of the boundary layer. The findings can be useful for object identification in underwater vehicles, and support the intriguing possibility that the significant viscous effects caused by nearby bodies on the fish boundary layer, far from preventing detection, could actually be used by animals to identify objects.

Key words: absolute/convective instability, biological fluid dynamics, boundary layers

1. Introduction

The development of smaller, inexpensive autonomous underwater vehicles is rapidly expanding with the emergence of new actuators, sometimes inspired by marine animals (Chu *et al.* 2012). The goal is to enable these vehicles to navigate the ocean and conduct complex tasks, such as inspecting offshore and submerged structures, and patrolling harbours autonomously. However, unlike the intricate sensory systems that allow aquatic animals to map their environment, currently available sensors for engineered vehicles, such as sonar, require large amounts of power and cannot fit in small spaces. Vision is not a reliable modality either, as underwater environments are often dark and turbid. To design more efficient and robust sensors, one can turn to the sensory systems of aquatic animals for inspiration.

† Email address for correspondence: maertens@mit.edu

In order to detect prey, predators or mates, and navigate through obstacles in the dark, fish can rely on several modalities: chemical sensing (Consi *et al.* 1994), electric sensing (MacIver, Fontaine & Burdick 2004) and flow sensing through their lateral line (Coombs & Montgomery 1999; Coombs *et al.* 2014). Because of its versatility, flow sensing is a very widely used modality. It can be used passively to detect moving bodies, or actively to detect stationary objects by exploiting the fish's own motion. Biotic or abiotic bodies can be identified, as well as flow features, including those generated by the fish itself. A prime example is the blind Mexican cave fish (*Astyanax fasciatus*) that is known to rely on its lateral line for most of its behaviours (Montgomery, Coombs & Baker 2001), including object detection and identification (von Campenhausen, Riess & Weissert 1981; Hassan 1986). Implementation of artificial lateral lines in underwater robots has already shown promising results such as station holding in a laboratory setting (Salumäe & Kruusmaa 2013). However, a fundamental understanding of the complex hydrodynamics at play is necessary to implement more complex and robust behaviours in unpredictable environments.

The lateral line consists of hundreds of flow sensing units, called neuromasts, located either directly on the fish skin, in direct contact with the flow, or embedded in canals connected to the external fluid through pores on the skin (Webb 2000). The surface neuromasts act as local flow velocity or skin friction sensors (McHenry, Strother & van Netten 2008). When the fish moves rapidly or is holding station in external flow, these sensors are believed to saturate and lose their sensitivity to perturbations (Engelmann, Hanke & Bleckmann 2002). The canal lateral line, identified as measuring pressure gradient, is considered to be the major subsystem involved in prey detection and obstacle identification (Coombs & Braun 2003). A convenient implementation of the canal subsystem consists of an array of pressure sensors (Salumäe & Kruusmaa 2013). As discussed by Windsor & McHenry (2009), the pressure remains constant across the thickness of the boundary layer, therefore previous studies relied on potential flow models ignoring viscous effects to estimate the pressure sensed by a fish. The inviscid flow theory can indeed very accurately model prey localization with a vibrating dipole (Ćurčić-Blake & van Netten 2006; Goulet *et al.* 2007).

A gliding fish can use its lateral line to sense changes in the patterns of its self-generated flow, caused by interaction with stationary obstacles (Windsor, Tan & Montgomery 2008). Hassan (1985) studied the disturbances caused by circular cylinders with a potential flow model, but viscous simulations of a fish gliding toward or parallel to a wall showed that viscous effects are substantial (Windsor *et al.* 2010*a*,*b*). Fernandez *et al.* (2011) showed that the flow disturbances caused by a stationary cylinder actively interact with the boundary layer of a sensing body, rendering potential flow predictions inaccurate. Despite some encouraging results obtained using a potential flow model in a Bayesian framework for cylinder identification (Fernandez *et al.* 2011), accuracy is limited because of the rapid breakdown of the potential flow model. While the difficulty of solving the Navier–Stokes equations makes their real-time application computationally infeasible, accounting for viscous effects is essential for accuracy.

In order to develop procedures to model the development of unsteady disturbances, we rely on methods of linear stability analysis that have proven effective in predicting the dominant features of unsteady flows, such as wakes (Triantafyllou, Triantafyllou & Chryssostomidis 1986; Oertel 1990) and separating boundary layers (Marquillie & Ehrenstein 2003). The methods are widely used to study the transition of airfoil boundary layers from laminar to turbulent (Reed, Saric & Arnal 1996), and can also

predict the selective intensification that occurs when certain disturbances interact with the boundary layer (Wu *et al.* 1999). In this paper, we show through a combination of experiments, potential flow and viscous two-dimensional flow simulations, that linear stability analysis can accurately model the interactions between the boundary layer of a foil and the flow disturbances caused by a circular cylinder. More specifically, we show that the boundary layer of the foil acts as a tuned amplifier whose properties can be predicted using open water flow results. The accuracy of the potential flow approximation can therefore be significantly improved by combining it with a linear amplifier whose properties depend only on the Reynolds number, and which models the boundary layer effects. Unlike previous work, such as Huerre & Monkewitz (1990) and Theofilis (2011), we consider how a signal of interest, as opposed to noise, is amplified by the boundary layer. By amplifying the disturbance caused by an object, the boundary layer could help fish detect and identify obstacles using their lateral line.

The model problem, the experimental set-up, and the numerical methods used are described in § 2. Specifically, the symbols and dimensionless numbers are defined in § 2.1, followed by a description of the experiments (§ 2.2) and the viscous (§ 2.3) and potential flow (§ 2.4) simulations. The methodology of the boundary layer linear stability analysis is presented in § 2.5. In § 3, we first describe the viscous effects on a foil passing an elliptical or circular cylinder (§§ 3.1 and 3.2). We then show that the boundary layer of the foil is subject to a convective instability that can amplify the pressure disturbances caused by a passing cylinder (§ 3.3) and present a method for incorporating this knowledge to improve potential flow predictions (§ 3.4 and appendix B). In § 4, we consider the implications of the results presented in § 3. In particular, we reconcile our results with the well accepted role of the boundary layer as a mechanical filter affecting the lateral line. (§ 4.1). Finally, we provide numerical results for the typical frequency of the disturbance along a blind Mexican cave fish, and discuss how the boundary layer instability could help fish detect (§ 4.2) and identify (§ 4.3) objects.

2. Materials and methods

We define a model problem with two-dimensional geometry to study the sensing mechanisms of a fish detecting an object: the gliding fish is modelled as a rigid foil of chord length L, while the object to be detected is represented by a stationary cylinder of elliptical or circular cross-section.

2.1. *Symbols and dimensionless numbers*

The Reynolds number is based on the foil length L and the foil gliding speed U_s as defined in figure 1, such that for kinematic viscosity ν, $Re = U_s L/\nu$. In the simulations, the reference frame is attached to the foil, and the free-stream $\boldsymbol{U_s} = U_s \boldsymbol{i_x}$ defines the positive $\boldsymbol{x}$ direction. All lengths are normalized by L, velocities by U_s and times by L/U_s. The results are presented in dimensionless units where the leading edge of the foil is located at $x = 0$, its trailing edge at $x = 1$ and $t = 0$ corresponds to the time when the centre of the cylinder is at $x = 0$. The pressure coefficient C_p is calculated from the pressure p such that $C_p = 2p/(\rho U_s^2)$, where the pressure is 0 at infinity. The average velocity field around the foil in open water is denoted $\boldsymbol{u_0}$ and the instantaneous velocity field is $\boldsymbol{u} = \boldsymbol{u_0} + \boldsymbol{u}'$. Similarly, the instantaneous pressure is decomposed as $p = p_0 + p'$. Here, $\mathscr{C}$ denotes a circular cylinder with radius r that passes at distance d from the foil (projected onto the y-axis). $\mathscr{C}_1$ is the cylinder characterized by $r = 0.1$ and $d = 0.1$.

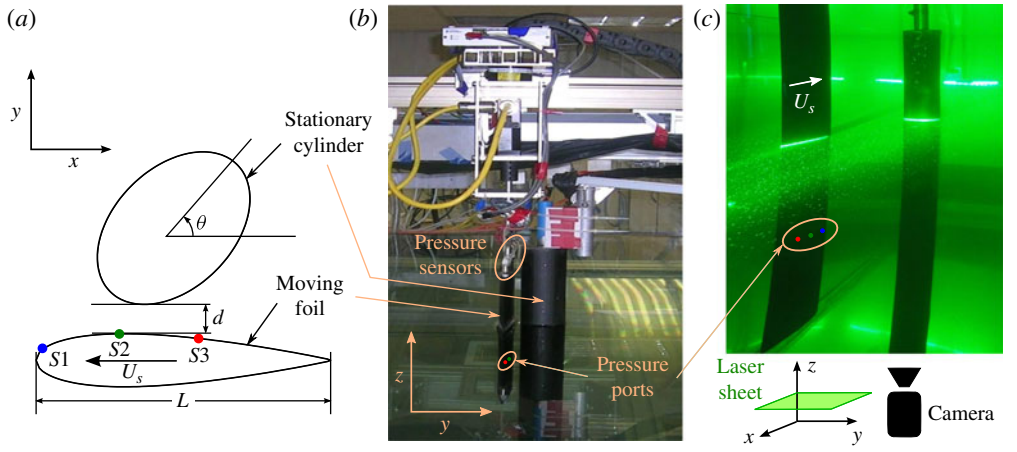

FIGURE 1. (Colour online) (*a*) Sketch of the cross-section of the experimental apparatus showing the location of the pressure ports (S1, S2 and S3). (*b*) Picture of the experimental set-up. (*c*) Picture showing the laser sheet in a particle tracking set-up.

2.2. *Towing tank experiments*

Experiments were conducted in the SMART (Singapore–MIT Alliance for Research and Technology) Centre testing tank in Singapore that has dimensions 3.6 m × 1.2 m × 1.2 m. A NACA0018 foil with chord length $L = 15$ cm and span $s = 60$ cm was towed past a stationary cylinder using an x–y gantry system supplied by Parker Engineering and controlled using Parker motor controllers and proprietary motion control software. The foil was cast with internal 3.18 cm PVC tubing to transmit pressure from taps at the foil midspan to the top. Honeywell 19C015PG4K pressure sensors were mounted on top of the foil, and measurements were collected at a sampling rate of 500 Hz via a NI USB-6289 data acquisition card. The experimental set-up and the location of the sensor ports are shown in figure 1.

The foil was towed at speed $U_s = 0.5$ m s^{-1} (corresponding to Reynolds number $Re = 75\,000$) past a stationary cylinder of circular or elliptical cross-section. At its closest point, the foil was $d = 5$–10 mm ($0.03L < d < 0.07L$) away from the cylinder. A laser sheet and particle tracking system were used to visualize the flow as shown in figure 1(*c*).

Note that the parameters used in the experiments do not match the values typically found in nature. Whereas blind cave fish are best modelled by foils of 12–13 % thickness (Windsor *et al.* 2010*a*), a thicker foil was necessary to fit the pressure sensors and tubing. The Reynolds number was one order of magnitude larger than values typically found in the cave fish to ensure a large signal-to-noise ratio. The effects of Reynolds number and foil thickness are at most moderate in this subcritical regime and do not change qualitatively the results.

2.3. *Viscous numerical simulations*

In order to map the entire velocity and pressure fields, we performed two-dimensional viscous simulations on a Cartesian grid using the boundary data immersion method (BDIM) described by Weymouth & Yue (2011) and Maertens & Weymouth (2014). In BDIM, the prescribed body kinematics and Navier–Stokes equations are integrated

over the fluid and solid domains with a kernel of finite radius ϵ. The resulting blended equations are valid over the complete domain and enforce the no-slip boundary condition at the fluid/solid interfaces. Problems previously studied with this robust immersed boundary method include ship flows and flexible wavemaker flows (Weymouth *et al.* 2006), shedding of vorticity from a rapidly displaced foil (Wibawa *et al.* 2012), and a cephalopod-like deformable jet-propelled body (Weymouth & Triantafyllou 2013). In Maertens & Weymouth (2014) we demonstrate the ability of BDIM to handle several moving bodies and generalize the original method to accurately simulate the flow around streamlined foils at Reynolds numbers of the order of $Re = 10^4$. The numerical details of the simulation method follow those in Maertens & Weymouth (2014) and are summarized in appendix A.

In the present simulations, the sensing vehicle is represented by a NACA0012 foil of unit length $L = 1$ attached to the computational frame, whereas a circular cylinder moves with the free stream and passes at a distance d from the foil as illustrated in figure 1. The computational domain extends $10L$ upstream of the foil, $12L$ downstream and $5.5L$ on either side. Constant velocity $\boldsymbol{u} = \boldsymbol{U}_s$ on the inlet, upper and lower boundaries and a zero gradient exit condition with global flux correction were used. The grid spacing was set to 200 points per chord length near the foil (corresponding to 24 points across the thickness of the foil) with a 1 % geometric expansion ratio for the grid spacing in the far-field.

Blind cave fish have typical lengths from $L = 5$ to 10 cm and swim at speeds between $U_s = 5$ and 15 cm s^{-1}, corresponding to Reynolds numbers exceeding $Re = 2500$ (Teyke 1988). In the present paper, Reynolds numbers ranging from 2000 to 20 000 are considered. Since the parameters in the simulations were chosen to match the values found in nature rather than those of the experiments, experimental and viscous simulated results will only be qualitatively compared (§§ 3.1 and 3.2).

2.4. *Potential flow model*

In order to calculate the potential flow approximation to the problem, we implemented in Matlab a two-dimensional constant source panel method. Using the same notation as in the previous sections, we consider a free-stream $\boldsymbol{U}_s$ and we denote by $\boldsymbol{V}$ the prescribed body velocity, which is a function of the location $\boldsymbol{x}$ for multiple or deforming bodies. $\boldsymbol{n}$ is the unit normal vector to the fluid/solid interface. The velocity potential Φ is decomposed as

$$\Phi(\boldsymbol{x}) = \boldsymbol{U}_s \cdot \boldsymbol{x} + \phi(\boldsymbol{x}), \tag{2.1}$$

and satisfies $\nabla^2 \Phi = 0$ in the fluid with the boundary conditions:

$$\begin{cases} \dfrac{\partial \phi}{\partial n} = (\boldsymbol{V} - \boldsymbol{U}_s) \cdot \boldsymbol{n} & \text{along the fluid/solid boundary,} \\ \nabla \phi = 0 & \text{at infinity.} \end{cases} \tag{2.2}$$

We solve this boundary-value problem by uniformly discretizing the periphery of each object. The foil and the cylinder were discretized into 200 and 50 segments, respectively.

If the viscous velocity field $\boldsymbol{v}$ is known, the potential flow model can be improved by moving the fluid/solid interface δ^* in the direction of its normal vector $\boldsymbol{n}$. Here, δ^* is the displacement thickness, calculated as

$$\delta^* = \int_0^{\delta} \left(1 - \frac{v(y)}{v(\delta)}\right) \mathrm{d}y, \tag{2.3}$$

where y is the distance to the boundary and v the component of $\boldsymbol{v}$ tangential to the boundary. δ is the overall thickness of the boundary layer, which we define as the distance y normal to the wall where

$$\frac{\mathrm{d}v}{\mathrm{d}y}(y) = 0.01\frac{\mathrm{d}v}{\mathrm{d}y}(0). \tag{2.4}$$

If the boundary layer velocity is approximated by its time average, a constant displacement thickness δ_0^* is used. In cases where the instantaneous displacement thickness $\delta^*(t)$ is used, the rate of change of the displacement thickness directly impacts the source strengths since the normal velocity of the boundary used in (2.2) is

$$\boldsymbol{V}\cdot\boldsymbol{n} = \boldsymbol{V_b}\cdot\boldsymbol{n} + \frac{\mathrm{d}\delta^*}{\mathrm{d}t} \tag{2.5}$$

where $\boldsymbol{V_b}$ denotes the solid body velocity. Therefore, viscous effects responsible for dynamic changes in the displacement thickness directly affect the pressure on the surface of the foil.

2.5. *Linear stability analysis of the boundary layer*

A gliding fish or a foil in steady motion develops a boundary layer and steady-state flow characterized by the velocity field $\boldsymbol{u_0}$ and pressure field p_0. This basic flow field satisfies the incompressible Navier–Stokes and continuity equations. The presence of a solid object in the neighbourhood of the foil causes a perturbation to that basic flow characterized by velocity field $\boldsymbol{u}'$ and pressure field p'. Writing the Navier–Stokes equation for the total flow field leads to the following disturbance equations:

$$\frac{\partial \boldsymbol{u}'}{\partial t} - \frac{1}{Re}\nabla^2\boldsymbol{u}' + (\boldsymbol{u_0}\cdot\nabla)\boldsymbol{u}' + (\boldsymbol{u}'\cdot\nabla)\boldsymbol{u_0} + (\boldsymbol{u}'\cdot\nabla)\boldsymbol{u}' + \nabla p' = 0, \tag{2.6a}$$

$$\nabla\cdot\boldsymbol{u}' = 0. \tag{2.6b}$$

Assuming that the radius of curvature is significantly larger than the boundary layer thickness, we can omit curvature effects. As discussed in Reed *et al.* (1996), inclusion of curvature and non-parallel effects improves the predictions only marginally. Assuming that the perturbation is small and keeping only the first-order terms, we get the linear disturbance equation for parallel flow. We then express the velocity field $\boldsymbol{u}'$ in terms of the streamline function that we write as a superposition of normal modes:

$$\psi(x, y, t) = \varphi(y)\mathrm{e}^{\mathrm{i}(kx-\omega t)} \tag{2.7}$$

where ω is a complex frequency and k a complex wavenumber. Their real parts ω_r and k_r represent the physical frequency and wavenumber of the disturbance, respectively, while their imaginary parts ω_i and k_i represent the time and space growth (or decay) rates, respectively. The resulting linearized disturbance equation is the Orr–Sommerfeld equation:

$$(u_0 - \omega/k)\left(\frac{\mathrm{d}^2}{\mathrm{d}y^2} - k^2\right)\varphi - \frac{\mathrm{d}^2u_0}{\mathrm{d}y^2}\varphi - \frac{\mathrm{i}}{k\,Re}\left(\frac{\mathrm{d}^4}{\mathrm{d}y^4} + 2k^2\frac{\mathrm{d}^2}{\mathrm{d}y^2} + k^4\right)\varphi = 0 \tag{2.8}$$

with boundary conditions $\varphi(y) = 0$ and $\mathrm{d}\varphi/\mathrm{d}y = 0$ at $y = (0, +\infty)$. Here, u is the component of $\boldsymbol{u}$ tangent to the boundary and y is the normal distance to the boundary. The pressure perturbation associated with mode φ is then given by

$$p(y) = (\omega/k - u_0)\frac{\mathrm{d}\varphi}{\mathrm{d}y} + \varphi\frac{\mathrm{d}u_0}{\mathrm{d}y} + \frac{\mathrm{i}}{k\,Re}\frac{\mathrm{d}}{\mathrm{d}y}\left(\frac{\mathrm{d}^2\varphi}{\mathrm{d}y^2} - k^2\varphi\right). \tag{2.9}$$

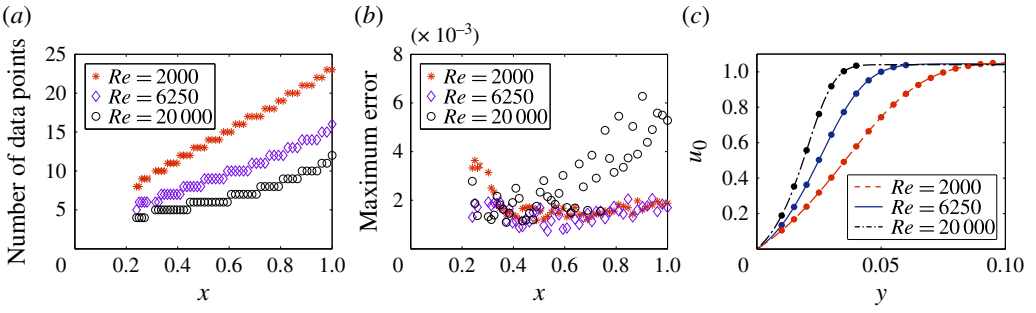

FIGURE 2. (Colour online) Boundary layer fit for $Re = [2000, 6250, 20\,000]$. (*a*) Number of data points used to fit each boundary layer profile. (*b*) Maximum error between the viscous simulation data points and the fitted profiles (normalized by U_e). (*c*) Boundary layer velocity profiles (solid lines) fitted from viscous simulations data points (•) at $x = 0.8$.

Re	U_e	δ_{99}	a	b	c
2000	1.054	0.094	0.741	1.123	0.841
6250	1.042	0.060	0.438	1.214	0.878
20 000	1.038	0.040	0.394	0.797	1.130

TABLE 1. Fitted parameters for the velocity profiles at $x = 0.8$.

We discretize (2.8) using Chebyshev polynomials, which are particularly well suited to solve the Orr–Sommerfeld equation (Orszag 1971), although other discretizations are also commonly used (Theofilis 2011). For a given wavenumber k, the corresponding eigenvalues ω and eigenmodes φ can be identified by solving the resulting eigenvalue problem. We used a Matlab code adapted from Weideman & Reddy (2000) to solve (2.8) with 128 points across a domain of length 1. The eigenvalue (frequency) with largest imaginary part corresponds to the most unstable mode, called principal mode. The frequency and wavenumber of principal modes are linked by the dispersion relation that we write $D(\omega, k, Re) = 0$.

The basic boundary layer is computed using the Navier–Stokes solver described in § 2.3. In order to easily compute the velocity and its derivatives at any point in the boundary layer, even at the wall where the immersed boundary method is least accurate, the maximum velocity U_e and boundary layer thickness δ_{99} are estimated and a profile of the form:

$$u_0(y) = U_e \tanh\left[a\frac{y}{\delta_{99}} + b\left(\frac{y}{\delta_{99}}\right)^2 + c\left(\frac{y}{\delta_{99}}\right)^3\right] \tag{2.10}$$

is fitted for each x location and Reynolds number. The number of data points used to fit the profiles and associated errors are shown in figure 2(*a*,*b*) for various Reynolds numbers and locations along the foil. Only locations $x > 0.3$ are shown as this ensures enough data points to properly fit the profile. Moreover, locations $x < 0.3$ will not be needed in this study (see figure 7 for instance). Examples of profiles at $x = 0.8$ are shown in figure 2(*c*) and the corresponding parameters can be found in table 1. These profiles are used to compute u_0 and its second-order derivative in (2.8).

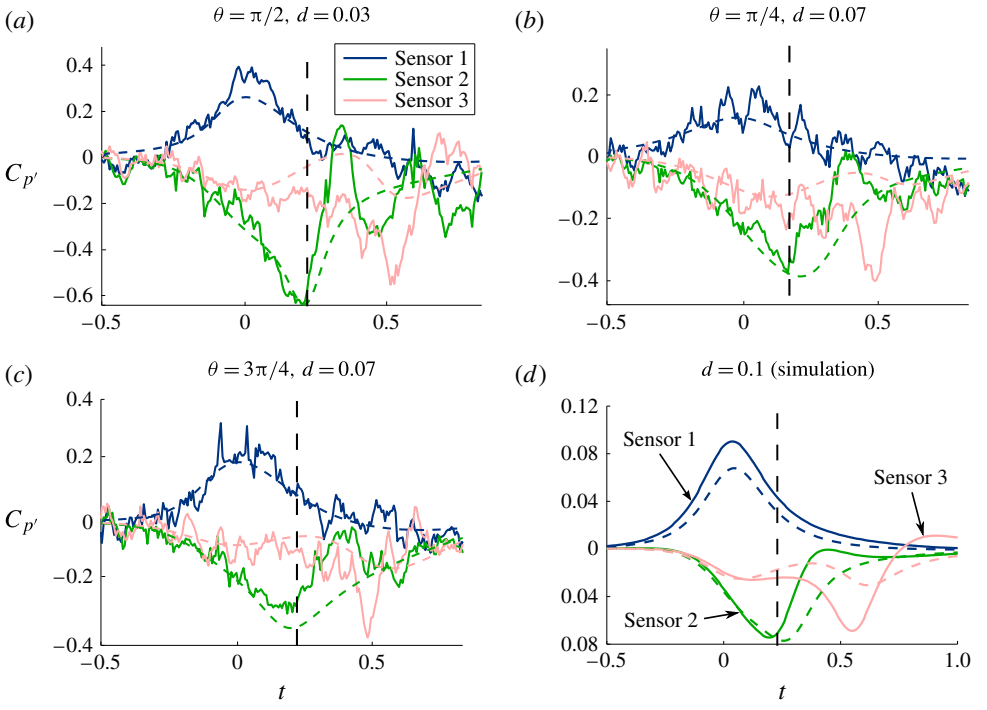

FIGURE 3. (Colour online) Pressure traces at the three sensor locations shown in figure 1. A vertical black dashed line at $t = 0.2$ shows a visual indication of when the potential flow pressure starts diverging from the viscous pressure. (*a–c*) Experimental (solid lines) and potential flow (dashed lines) traces for a NACA0018 ($Re = 75\,000$) passing an elliptical cylinder at various orientations θ and distances d indicated on the plots. The ellipse has major radius 0.3 and minor radius 0.2. (*d*) Traces from viscous (solid lines) and potential flow (dashed lines) simulations of a NACA0012 ($Re = 6250$) passing cylinder $\mathscr{C}_1$ ($r = 0.1$, $d = 0.1$). In the potential flow simulation of (*d*) only, the foil has been augmented by its displacement thickness δ_0^* (it is much thinner and not exactly known in the experimental cases).

3. Results

3.1. *Viscous and inviscid pressure traces*

We first compare pressure traces recorded in the experiments and those simulated with BDIM with potential flow estimates. Figure 3(*a–c*) shows traces of the pressure at the three sensor locations indicated in figure 1(*b*) as the NACA0018 passes an elliptical cylinder at three different orientations. For all orientations, as the foil passes the cylinder ($0 < t < 1$), significant differences arise between the pressure recorded by the sensors and the inviscid theory predictions.

The value of the pressure coefficient measured by the first sensor increases as the foil approaches the cylinder and slowly returns to its initial value after $t = 0$. A displacement of the stagnation point toward the cylinder is responsible for the pressure increase and this pressure trace is similar to what would be expected from an inviscid fluid.

The pressure measured by the second sensor decreases as it approaches the cylinder and the fluid accelerates as it has to go through the channel formed by the foil and

the cylinder. Once the sensor has passed the cylinder ($t \approx 0.2$), the potential flow model predicts that the pressure slowly returns to its initial value. However, the experimentally measured pressure recovers much faster, before undergoing potentially large oscillations. This feature, consistently observed across all experiments, cannot be accounted for by the potential flow theory.

At the third sensor location, the potential flow model predicts that the pressure slightly decreases as the foil approaches the cylinder, which is experimentally observed. After the front of the foil has passed the cylinder ($t \approx 0$), the inviscid model predicts that the pressure returns to its initial value, before slightly decreasing and increasing again as the sensor passes the cylinder. The experimental pressure, however, keeps decreasing until the sensor passes the cylinder ($t \approx 0.5$), and only then does it rapidly recover its initial pressure. As has been observed for the second sensor, the experimentally measured pressure roughly matches the inviscid pressure until the second sensor passes the cylinder ($t \approx 0.2$), but afterwards the two pressures differ significantly.

The experiments have shown consistently similar results for various orientations of the ellipse. In figure 3(*d*) we compare the pressure traces calculated by the viscous code with potential flow estimates for the circular cylinder $\mathscr{C}_1$ at $Re = 6250$. Despite differences in the cylinder size and geometry, and the Reynolds number and foil thickness, the viscous pressure traces present the same features as observed in the experiments. The mechanism responsible for the discrepancy between an ideal and a viscous fluid appears to have only a weak dependence on the geometry and Reynolds number. Therefore, results from the present case are assumed to be representative of most configurations and will be used in the remaining part of this study to illustrate the discussion.

3.2. *Flow field around a foil passing a cylinder: viscous effects*

Figure 4(*a*,*b*) shows the velocity and pressure coefficient fields at two different times for a NACA0012 passing near the cylinder $\mathscr{C}_1$ ($r = 0.1$, $d = 0.1$) at $Re = 6250$. The presence of the cylinder deflects the streamlines, and in particular, figure 4(*a*) shows that at $t = 0.3$ the flow between the foil and the cylinder is accelerated and the pressure decreased. In order to better visualize the changes due to the cylinder, figure 4(*c*,*d*) shows the instantaneous velocity and pressure fields from which the steady state has been subtracted. At $t = 0.3$, the cylinder pushes the flow near the leading edge toward the upstream direction, resulting in a stagnation point shifted toward $y > 0$ and an increase in pressure on the cylinder side. Just downstream of the cylinder, the flow is accelerated toward the trailing edge, resulting in a faster flow and therefore a decrease in pressure. As the cylinder moves downstream ($t = 0.9$), the cylinder keeps accelerating the flow between itself and the foil, causing a decrease in pressure. Even though the pressure drop near the cylinder is much weaker at $t = 0.9$ than at $t = 0.3$, the amplitude of the pressure drop on the foil is not reduced significantly. Upstream of the low-pressure region on the foil, there is also a high-pressure region ($x \approx 0.55$) that does not appear to be directly caused by the cylinder.

While in figure 4(*e*) magnification does not reveal any additional features, figure 4(*f*) shows a pair of counter-rotating vortices in the foil boundary layer, around $x = 0.55$ and $x = 0.8$. These vortices correspond to the high- and low-pressure areas along the foil and are responsible for the discrepancies observed earlier between viscous and inviscid pressure predictions. Similarly, swirling flow along the rear half of the foil passing near a cylinder has been observed experimentally, as illustrated in figure 5.

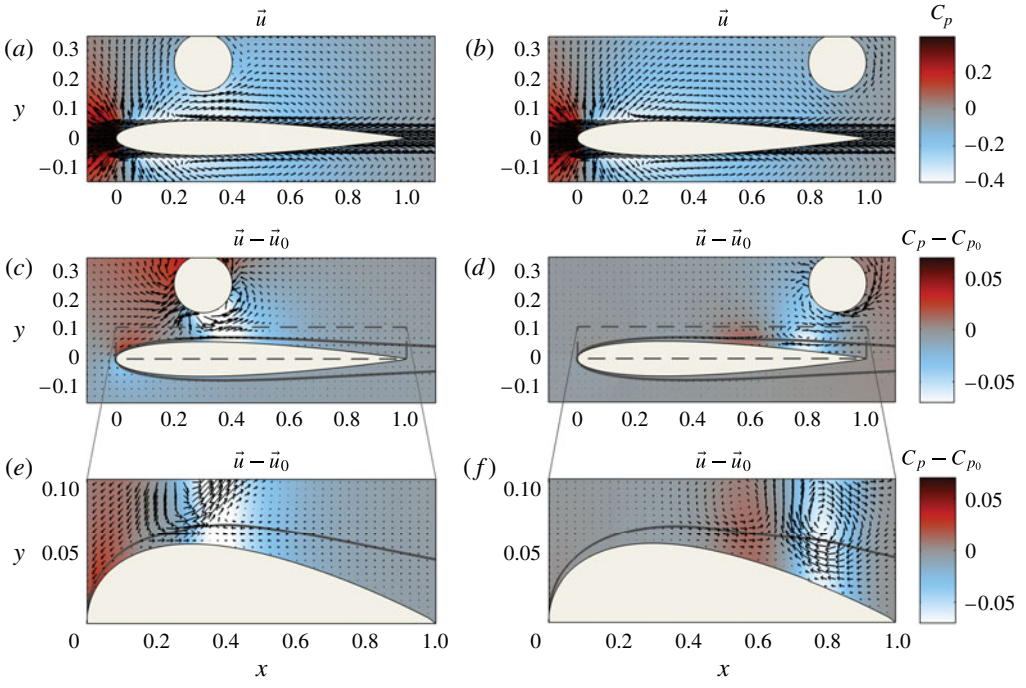

FIGURE 4. (Colour online) Snapshots at $t=0.3$ (a,c,e) and $t=0.9$ (b,d,f) as a NACA0012 foil passes near the cylinder $\mathscr{C}_1$ ($r=0.1$, $d=0.1$) at $Re=6250$. (a,b) Velocity field and pressure coefficient. (c,d) The steady fields $\boldsymbol{u_0}$ and C_{p_0} have been subtracted and the displacement thickness $\delta^*(t)$ is shown by a solid grey line. (e,f) Magnified view of the area enclosed within the dashed line of (c,d).

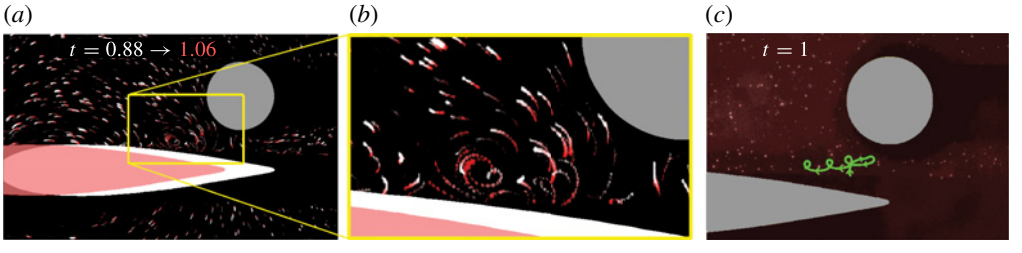

FIGURE 5. (Colour online) Experimental flow visualization as a NACA0018 foil passes near a cylinder at $Re=75\,000$. (a,b) Particles pathlines from $t=0.88$ to $t=1.08$. The locations of the foil at the start and end times are represented with their respective colour (the intersection is shown by an intermediate colour). (b) Magnified view of the swirling flow region. (c) A representative pathline from $t=0.1$ to $t=1$ is represented with arrows showing the direction of motion.

The presence of vortices implies that the pressure changes along the surface of a foil passing close to a cylinder, cannot be accounted for solely by inviscid theory. A second component, resulting from the boundary layer dynamics and containing memory effects, is needed to complement the potential flow model. We argue that if the changes in the boundary layer thickness are known, a potential flow

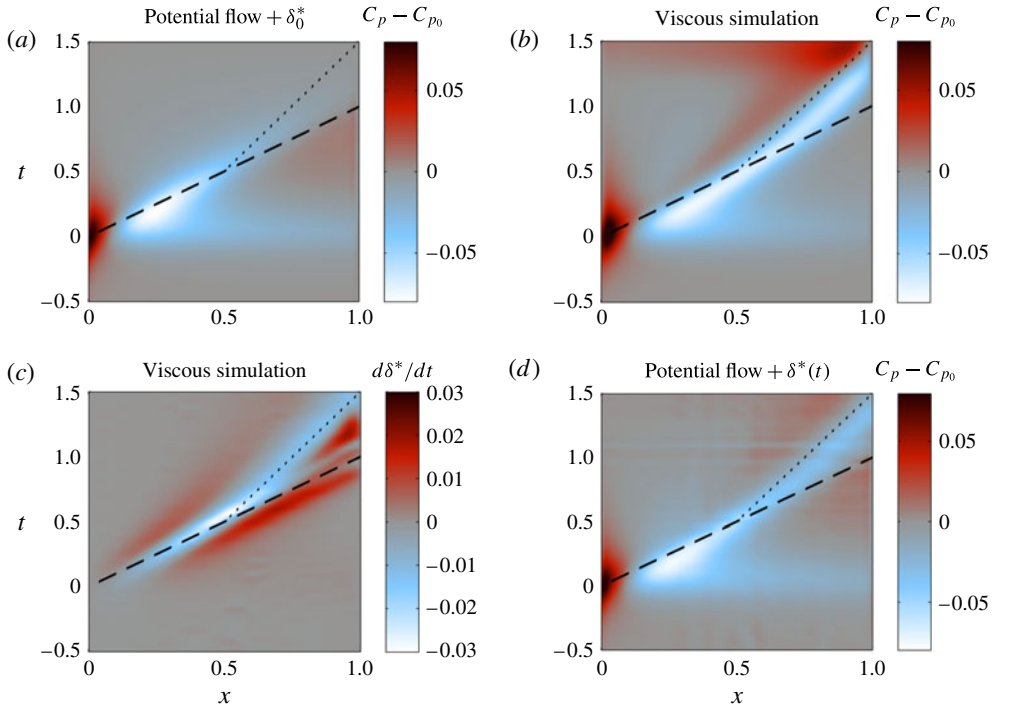

FIGURE 6. (Colour online) (*a*,*b*,*d*) Pressure coefficient changes along a NACA0012 foil passing near the cylinder $\mathscr{C}_1$ at $Re = 6250$, as a function of space and time: (*a*) calculated from potential flow using the steady-state displacement thickness; (*b*) calculated with the Navier–Stokes solver; (*d*) calculated from potential flow using the instantaneous displacement thickness. (*c*) Rate of change of displacement thickness. Dashed line: cylinder location projected onto the *x*-axis; dotted line: location of a hypothetical feature moving along the foil at half the free stream.

model accounting for them can provide pressure predictions in good agreement with experiments and viscous simulations.

Figure 6(*a*) shows the pressure changes along the foil passing near the cylinder $\mathscr{C}_1$ as a function of time and space, simulated with the potential flow code, augmenting the foil thickness by its steady-state boundary layer displacement thickness at $Re = 6250$. Vertical sections of this plot at $x = [0.03, 0.3, 0.57]$ would result in the pressure traces of figure 3(*d*). As has been discussed previously, the cylinder causes an increase in pressure near the leading edge, followed by a decrease in pressure around the thickest part of the foil. Along the thinner rear half of the foil, the pressure changes are much weaker.

Comparing the corrected potential flow prediction with the viscous simulation of figure 6(*b*), we see very good agreement downstream of the cylinder, but very poor agreement upstream of it. A strong low-pressure region moving at about half the free stream (dotted line) characterizes the viscous pressure changes along the rear half of the foil (top right quadrant). The amplitude of this secondary contribution to the pressure changes varies with Reynolds number and cylinder geometry, but it is noteworthy that it moves at about half the free-stream velocity for all of the cases we have tested. In order to assess how much improvement to the potential flow model

can be gained from knowledge of the boundary layer dynamics, the instantaneous displacement thickness has been estimated from the viscous simulations.

Figure 6(*c*) shows the rate of change of displacement thickness as a function of space and time. Here again, we can distinguish two components: a direct contribution from the cylinder following its displacement (dashed line), and a delayed contribution moving at half the free stream (dotted line). Even though the velocities involved are only a few per cent of the free-stream velocity, their contribution to the local source strength can be significant, as they are normal to the boundary. In other words, although the boundary layer thickness $\delta^*(t)$ does not vary much, its changes result in additional sources and sinks that significantly impact the pressure field.

Finally, in figure 6(*d*) we show the pressure changes estimated from the potential flow using the instantaneous displacement thickness $\delta^*(t)$. Even though the amplitude is slightly underestimated, the potential flow model is now able to predict the main features observed on figure 6(*b*), including the low-pressure region moving at half the free stream. This confirms our hypothesis that if the changes in the boundary layer thickness are known, a potential flow model accounting for them can provide pressure predictions in good agreement with viscous simulations.

3.3. *Convective instability in the foil boundary layer*

In the previous section, we showed that the discrepancy between the inviscid and viscous pressure estimates can be accounted for by the dynamics of the boundary layer. In this section we show that these dynamics can be predicted simply from the average shape of the foil boundary layer in open water flow. In particular, we explain why the secondary perturbation always moves at half the free-stream velocity and discuss the effects of the Reynolds number.

As described in § 2.5, the Orr–Sommerfeld equation identifies the eigenvalues ω and eigenmodes φ for a given boundary layer profile and wavenumber k. A boundary layer profile is unstable if for a real wavelength k_r, the imaginary part of the eigenvalue corresponding to its principal mode, ω_i, is positive. The boundary layer acts as an amplifier for the selected waves that grow exponentially in time while travelling with phase velocity $c_r = \omega_r/k_r$ and group velocity $c_g = \partial\omega_r/\partial k_r$ determined by the dispersion relation $D(\omega, k, Re) = 0$.

Figure 7(*a–c*) shows isocontour plots of positive ω_i as a function of space and wavelength. At $Re = 2000$, only the posterior 10 % of the foil boundary layer is unstable for wavenumbers between 10 and 20. However, as the Reynolds number increases, the unstable region grows larger and encompasses more wavenumbers. At Reynolds number 20 000, as much as half of the foil boundary layer span is unstable and the most unstable wavenumbers are between 30 and 40. For all three Reynolds numbers, unstable waves are convected downstream as they grow in time, which is referred to as convective instability (Bers 1983).

A wave with wavelength $2\pi/k$ and initial amplitude $A_0(k)$ at onset time t_0 and position x_0, has amplitude $A(k, t, x)$ as it evolves in time and propagates downstream. The amplitude ratio a is given by

$$\begin{aligned} a\big(k, t, x(t)\big) &= A/A_0 = \exp\left[\int_{t_0}^{t} \omega_i\big(k, \tau, x(\tau)\big)\,\mathrm{d}\tau\right] \\ &= \exp\left[\int_{x_0}^{x} \omega_i\big(k, t(\xi), x\big)/c_g\,\mathrm{d}\xi\right]. \end{aligned} \tag{3.1}$$

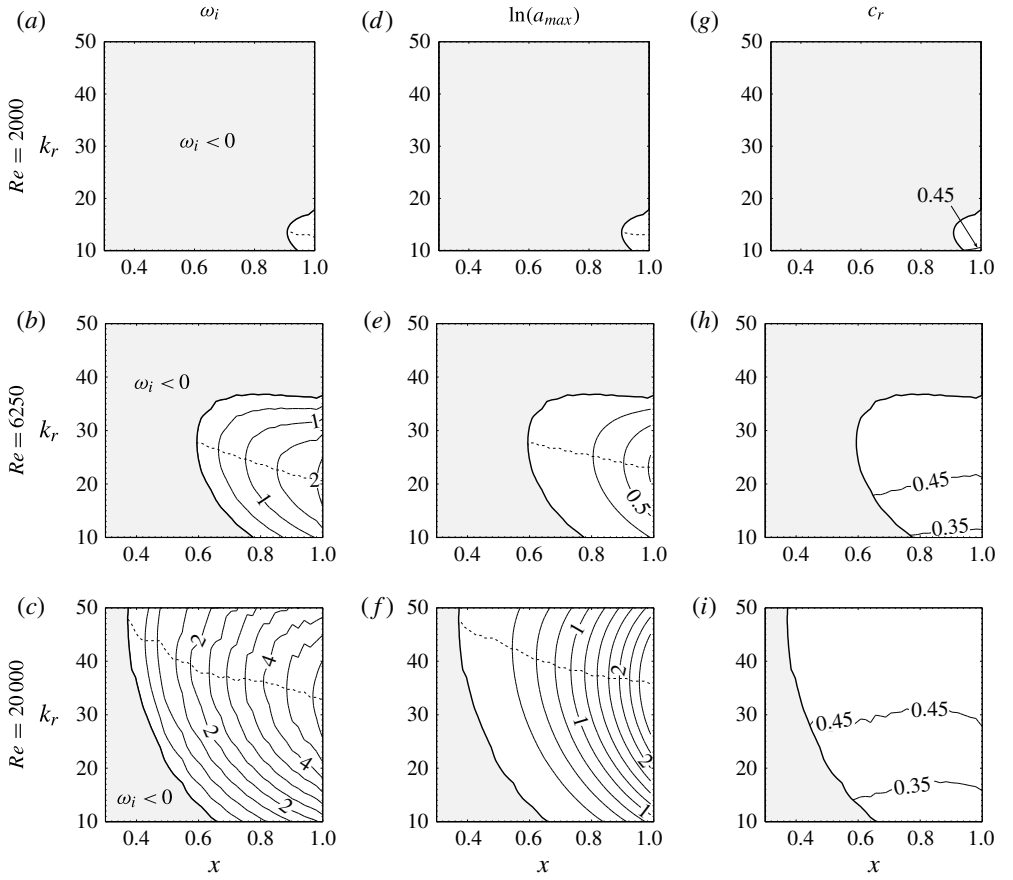

FIGURE 7. Properties of the mean boundary layer velocity profiles computed from viscous simulations, as a function of the location along the foil and wavenumber. (*a–c*) Isocontours of positive ω_i for the principal modes (0.5 between successive contours). The dotted line shows the most unstable wavenumber at each location. (*d–f*) Isocontours of the maximum amplification in logarithmic scale (0.25 between successive contours). The dotted line shows the wavenumber of largest a_{max} at each location. (*g–i*) Isocontours of the group velocity (0.1 between successive contours).

So if we denote by $x_1(k)$ the location where $\omega_i(k) = 0$, the maximum amplification is

$$a_{max}(k, x) = \max(A/A_0) = \exp\left[\int_{x_1}^{x} \omega_i(\xi, k)/c_g \, \mathrm{d}\xi\right]. \tag{3.2}$$

Figure 7(*d–f*) shows isocontours of positive a_{max}. Similarly to what has been observed in figure 7(*a–c*), as the Reynolds number increases, the unstable region starts earlier in space and encompasses a wider frequency range. At Reynolds number 2000, the most amplified wavenumber at the trailing edge is approximately 13 but a_{max} remains small (less than 1.1). At $Re = 6250$, the most amplified wavenumber at the trailing edge is close to 23 and a_{max} is now approximately 2. At Reynolds number 20 000, the most amplified wavenumber is 36 with a_{max} now greater than 12. When the foil passes near a cylinder, principal modes of its boundary layer get excited with an amplitude depending on the cylinder size and distance. The unstable modes are

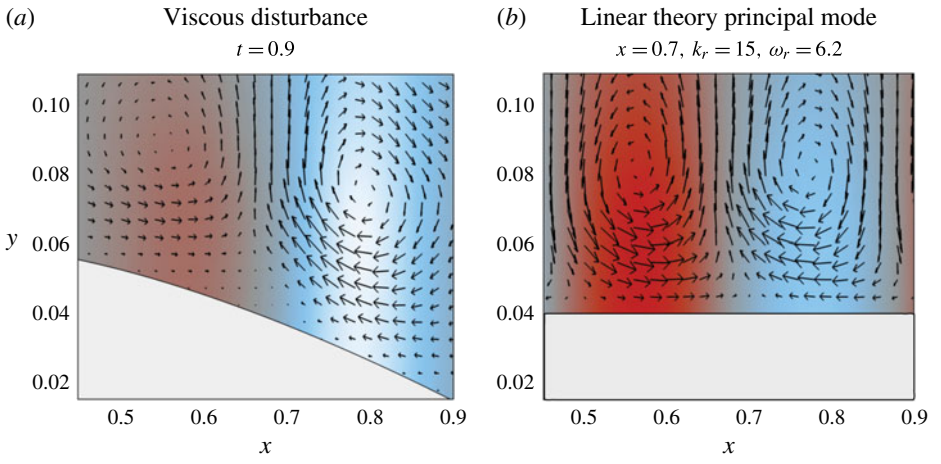

FIGURE 8. (Colour online) (*a*) Pair of counter-rotating vortices observed in the boundary layer of a NACA0012 passing near the cylinder $\mathscr{C}_1$ at $Re = 6250$. Arrows show the disturbance to the velocity field and colours the perturbation to the pressure field (the colour scale is the same as in figure 4*f*). (*b*) Principal mode for $x = 0.7$ and $k_r = 15$ shown above a boundary located at $y = 0.04$. The colour scale has been chosen to roughly match that of (*a*).

amplified and propagate at the velocity determined by the dispersion relation, resulting in the secondary perturbation observed in § 3.2.

Since for the range of Reynolds numbers considered disturbances with certain wavenumbers will grow faster (exponentially, due to the instability of the boundary layer) than with other wavenumbers, figure 7(*d–f*) shows that the boundary layer acts as a wavenumber-selective signal amplifier. The amplification rate and preferred frequency range strongly depend on the Reynolds number: the larger the Reynolds number, the larger the frequency and amplification rate. There is, however, one property of the boundary layer that remains constant across our range of Reynolds numbers: the phase velocity of the amplified waves. As shown in figure 7(*g–i*), the phase velocity of the most unstable modes is always between 0.45 and 0.55, explaining the observation made earlier that the secondary perturbation moves at half the free-stream velocity.

In figure 8(*a*) we show a close-up of the pair of counter rotating vortices observed in figure 4(*f*) in the boundary layer of the NACA0012 foil. Next to it, in figure 8(*b*), is shown the principal mode from the linear theory at $x = 0.7$ for $k_r = 15$ ($Re = 6250$). Despite the finite angle of the airfoil boundary with respect to the free-stream and a noticeable difference between the strength of the two vortices in figure 8(*a*), this figure is strikingly similar to figure 8(*b*). This similarity is another indication that despite the approximations employed, the linear stability theory is able to capture the dynamics of the boundary layer responsible for the secondary pressure perturbation. As observed by Chomaz (2005), linear stability theory has been shown 'by serendipity' to provide accurate predictions of the frequency and wavenumber of basically nonlinear flows. This proves once more to be the case in this problem.

Finally, figure 9 illustrates how the boundary layer properties discussed above impact the pressure distribution along a foil passing near a cylinder. Similarly to figure 6(*b*), figure 9 shows the pressure changes along the foil passing near the

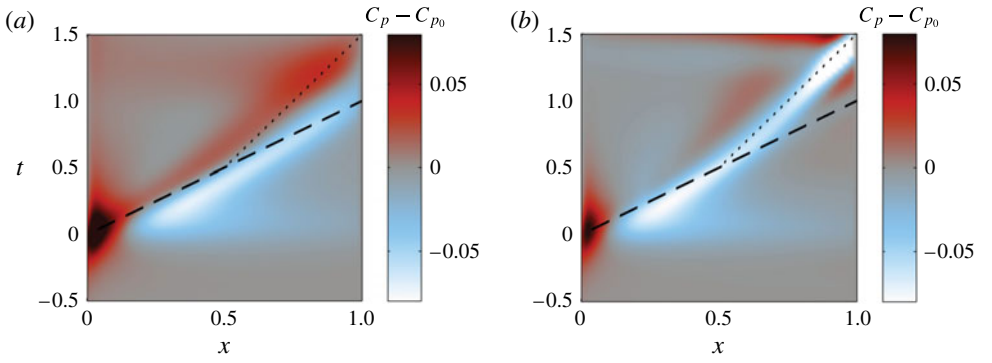

FIGURE 9. (Colour online) Viscous simulations of pressure coefficient changes as a function of time t and space x along a NACA0012 foil passing near the cylinder $\mathscr{C}_1$ for (*a*) $Re = 2000$ and (*b*) $Re = 20\,000$. Dashed line: cylinder location projected onto the x-axis; dotted line: location of a hypothetical feature moving along the foil at half the free stream.

cylinder $\mathscr{C}_1$, now at Reynolds number $Re = 2000$ and 20 000. The primary disturbance, in the bottom half of the figure, is very similar for both Reynolds numbers, but the secondary perturbation, characterized by a low pressure in the top right quadrant, changes with Reynolds number. Whereas at $Re = 2000$ the secondary perturbation is small, at $Re = 20\,000$ the amplification is such that by the time the instability reaches the trailing edge, its amplitude is larger than the disturbance that caused it.

3.4. *Enhancing potential flow predictions with instability results*

We have shown that the pressure changes along a foil passing near a cylinder have two main components: the first part can be approximated accurately by potential flow model, while the second part can be accounted for by the dynamics of the boundary layer, acting as an amplifier. The properties of the latter can be predicted from the average boundary layer shape in open water, but the resulting convective instability amplifies the features of the unsteady flow initially predicted by inviscid theory.

Let us consider a cylinder $\mathscr{C}$ causing a change in pressure coefficient $C_{p'}(x, t, \mathscr{C})$. We denote by $\tilde{p}(k, t, \mathscr{C})$ the discrete Fourier transform of $C_{p'}$ from the space to the wavenumber domain, using for our numerical results 128 points. We decompose the pressure changes into two components:

$$\tilde{p}(k, t, \mathscr{C}) = \tilde{p}_1(k, t, \mathscr{C}) + \tilde{p}_2(k, t, \mathscr{C}). \tag{3.3}$$

If we denote by $\tilde{p}_i$ the pressure changes estimated by inviscid theory augmenting the foil by δ_0^*:

$$\tilde{p}_1(k, t, \mathscr{C}) \simeq \tilde{p}_i(k, t, \mathscr{C}). \tag{3.4}$$

Following linear stability analysis, the secondary pressure changes can be approximated by

$$\tilde{p}_2(k, t, \mathscr{C}) \simeq \tilde{p}_i(k, t_0, \mathscr{C}) \exp\left(\int_{t_0}^{t} \omega_i(k, \tau)\, \mathrm{d}\tau\right) \mathbb{1}_{t>t_0} \simeq \tilde{p}_i(k, t_0, \mathscr{C})\, a(k, t) \tag{3.5}$$

for an appropriate time t_0. This expression is valid until the disturbances reach the trailing edge and are shed into the wake.

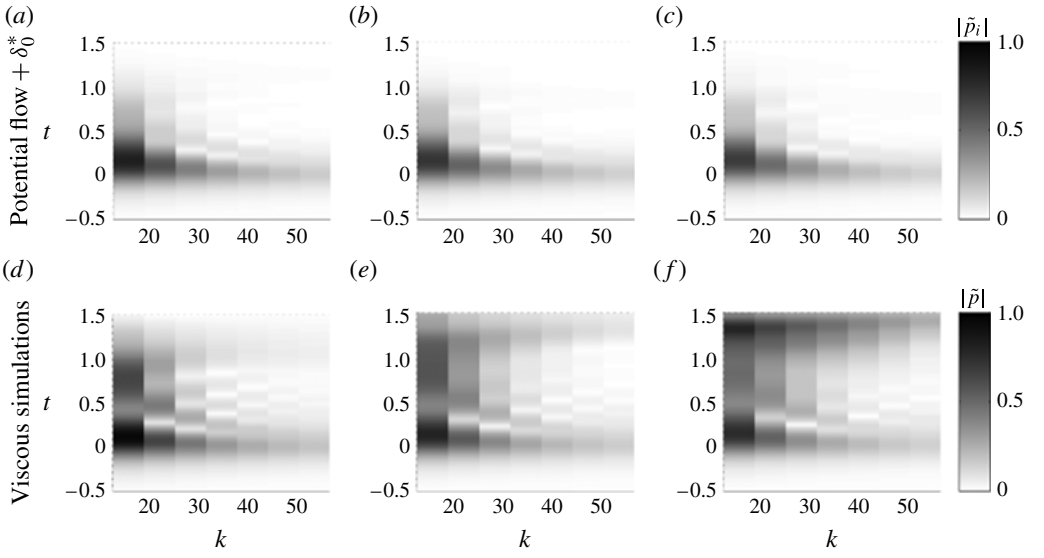

FIGURE 10. Pressure coefficient changes along a NACA0012 foil passing near the cylinder $\mathscr{C}_1$, as a function of wavenumber and time, for three Reynolds numbers, (*a*,*d*) $Re = 2000$, (*b*,*e*) $Re = 6250$ and (*c*,*f*) $Re = 20\,000$: (*a–c*) $|\tilde{p}_i(k, t, \mathscr{C})|$ inviscid simulation; (*d–f*) $|\tilde{p}(k, t, \mathscr{C})|$ viscous simulation. Resolution in the wavenumber domain is limited to 2π.

Using simulations for cylinders ranging in radius from 0.025 to 0.8 and placed at distances ranging from 0.05 to 0.8 (see appendix B), an estimated amplification coefficient $\hat{a}(k, t)$ has been calculated, where

$$|\tilde{p}(k, t, \mathscr{C}) - \tilde{p}_i(k, t, \mathscr{C})| = \hat{a}(k, t)|\tilde{p}_i(k, t_0, \mathscr{C})| + \epsilon. \tag{3.6}$$

Here, $t_0 = 0.15$ has been chosen, which roughly corresponds to the time when the amplitude of the inviscid disturbance reaches its maximum. Equations such as (3.6) are referred to as varying-coefficient models, which arise in many scientific areas, and numerous algorithms have been developed in the last 20 years to estimate their parameters (Hastie & Tibshirani 1993; Fan & Zhang 1999). The main advantage of these models over the more general form

$$\tilde{p}(k, t, \mathscr{C}) = f(k, t, \tilde{p}_i(k, t, \mathscr{C}), \tilde{p}_i(k, t_0, \mathscr{C})) + \epsilon \tag{3.7}$$

is that they can handle large dimensions, especially when their use is physically motivated as here. Details about varying-coefficient models and the algorithm used to estimate $\hat{a}(k, t)$ are found in appendix B.

Figure 10 shows the pressure coefficient changes along a NACA0012 foil passing near the cylinder $\mathscr{C}_1$, as a function of the wavenumber k and time t, for three Reynolds numbers 2000, 6250 and 20 000. Note that since the length of the foil is $L = 1$, the resolution in the wavenumber domain is limited to 2π. As in the space domain plots, the potential flow pressure changes shown in figure 10(*a–c*) are similar for all Reynolds numbers and are only measurable as the cylinder passes the front half of the foil ($0 < t < 0.5$). The viscous simulations shown in figure 10(*d–f*) predict a

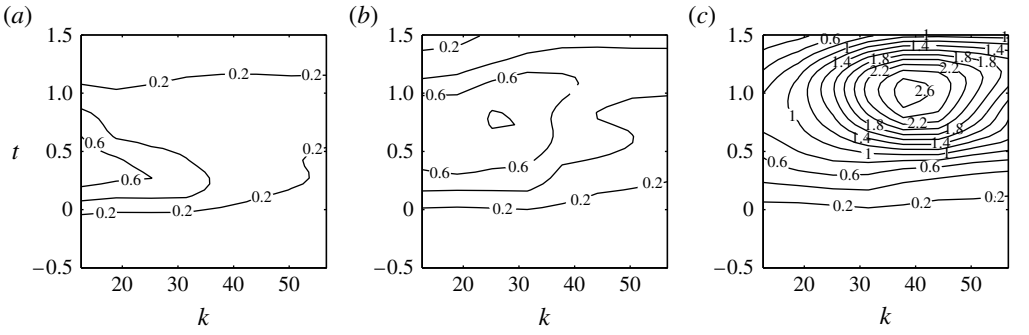

FIGURE 11. Amplification coefficient $\hat{a}(k, t)$ estimated from viscous simulations as a function of wavenumber and time for (*a*) $Re = 2000$, (*b*) $Re = 6250$ and (*c*) $Re = 20\,000$.

distinctive second component to pressure changes that appears later in time, is stronger in magnitude, and spans a wider range of wavenumbers for larger Reynolds numbers.

Figure 11 shows isocontours of the estimated coefficient $\hat{a}(k, t)$ for three Reynolds numbers. The results are consistent with the observations from § 3.3: the higher the Reynolds number, the larger the amplification rate and the value of the most amplified wavenumber are. The values of the most amplified wavenumbers are also very close to those predicted by linear theory: around $k = 18$ at $Re = 2000$, $k = 26$ at $Re = 6250$ and $k = 37$ at $Re = 20\,000$. The values found for amplification, however, are much smaller than the upper bound a_{max} found from linear theory and plotted in figure 7(*d–f*). Whereas according to the linear stability theory $\hat{a}(k, t)$ could reach 2 for $Re = 6250$ and 10 for $Re = 20\,000$, the values found here do not exceed 1 and 3, respectively. This difference can be explained by the fact that pressure changes near the leading edge of the foil largely contribute to $\tilde{p}_i(k, t_0, \mathscr{C})$, whereas they do not contribute much to $\tilde{p}_2(k, t_0, \mathscr{C})$ due to the high stability of the boundary layer near the leading edge.

We define the test error as the average value of the residual ϵ as defined by (3.6), calculated on a test set randomly chosen from the available data set and not used to estimate $\hat{a}(k, t)$. The remaining part of the data is referred to as the training set (see appendix B for details). Table 2 shows the average and standard deviation of the inviscid and viscous pressure changes for three Reynolds numbers and compares the test error to the difference between the viscous and potential flow models. While the magnitude of the inviscid perturbation decreases with increasing Reynolds number due to a thinner boundary layer, increased boundary layer instability induces a larger viscous disturbance. As a result, even after using the steady displacement thickness, the average error in the potential flow model is between 65 and 80 %. By adding the Reynolds number dependent component $\hat{a}(k, t)|\tilde{p}_i(k, t_0, \mathscr{C})|$ to the model, we are able to reduce the error substantially, bringing it down to values between 25 and 40 %.

Figure 12 compares the viscous residual $|\tilde{p}(k, t, \mathscr{C}) - \tilde{p}_i(k, t, \mathscr{C})|$ (figure 12*a–c*) to the fitted function $\hat{a}(k, t)|\tilde{p}_i(k, t_0, \mathscr{C})|$ (figure 12*d–f*). The simple form of (3.6) is able to enhance the potential flow model and reproduce the basic Reynolds number dependent features. In particular, the increased amplification of high frequencies and increased delay of the secondary perturbation at high Reynolds number are captured by the model. The memory and amplification effects due to the boundary layer are thus added to the inviscid perturbation without significant complexity. Thanks to its simplicity and the wide range of cylinder sizes and distances used to fit it, the model is likely to generalize well to other obstacle shapes. A more complex model could, however, achieve better quantitative agreement with the viscous simulations.

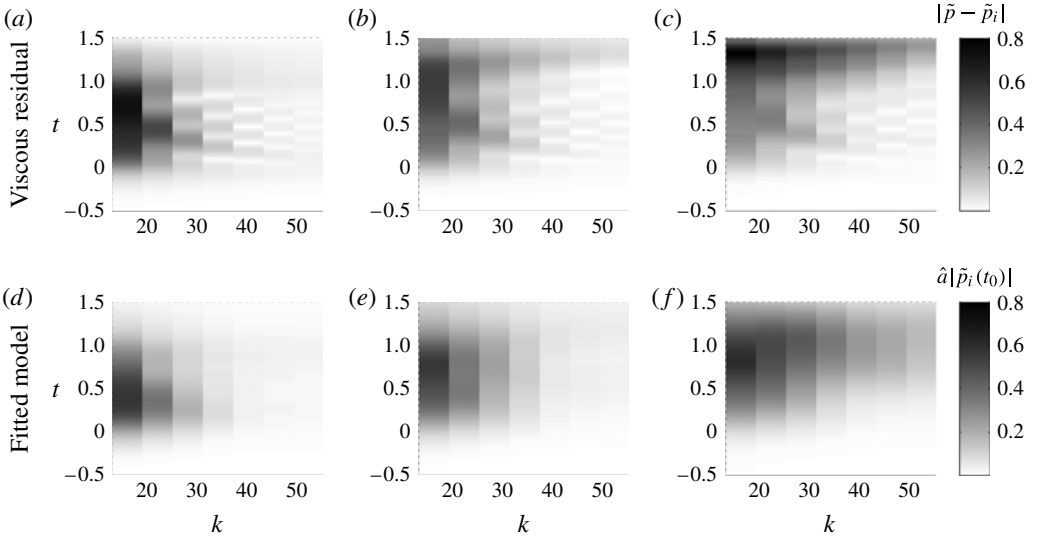

FIGURE 12. Pressure coefficient changes along a NACA0012 foil passing near the cylinder $\mathscr{C}_1$, as a function of wavenumber and time, for three Reynolds numbers, (*a*,*d*) $Re = 2000$, (*b*,*e*) $Re = 6250$ and (*c*,*f*) $Re = 20\,000$. (*a–c*) Viscous residual $|\tilde{p}(k, t, \mathscr{C}) - \tilde{p}_i(k, t, \mathscr{C})|$, (*d–f*) fitted model $\hat{a}(k, t)|\tilde{p}_i(k, t_0, \mathscr{C})|$. Resolution in the wavenumber domain is limited to 2π.

Re	2000	6250	20 000
$\lvert\tilde{p}_i\rvert$	0.123 (±0.009)	0.096 (±0.007)	0.092 (±0.006)
$\lvert\tilde{p}\rvert$	0.149 (±0.008)	0.168 (±0.008)	0.251 (±0.010)
$\lvert\tilde{p} - \tilde{p}_i\rvert/\lvert\tilde{p}\rvert$	0.668 (±0.051)	0.704 (±0.032)	0.772 (±0.018)
$\lvert\epsilon\rvert/\lvert\tilde{p}\rvert$	0.272 (±0.016)	0.284 (±0.015)	0.389 (±0.020)
$\lvert\epsilon\rvert/\lvert\tilde{p} - \tilde{p}_i\rvert$	0.409 (±0.025)	0.404 (±0.017)	0.504 (±0.025)

TABLE 2. Average and standard deviation of the training data set inputs and test error.

4. Discussion

4.1. *The boundary layer: filter or amplifier?*

We showed that the fish boundary layer acts as an amplifier of the pressure disturbance caused by a nearby cylinder. In the lateral line literature, the boundary layer is often viewed as a filter (McHenry *et al.* 2008), damping mostly low frequencies. The two views, however, are not contradictory as they refer to different problems.

The superficial neuromasts are located on the skin of the fish, contained within the boundary layer. Therefore, the measured velocity is attenuated depending on the ratio of neuromast height to boundary layer thickness. When the fish is stationary, the thickness of the boundary layer that develops due to an external stimulus reduces with increasing stimulus frequency; hence the boundary layer acts as a high-pass filter for the superficial neuromast excitation (McHenry *et al.* 2008). The neuromasts located inside the canals have been shown to respond to the gradient of pressure below typically a few hundred Hertz (van Netten 2006). In the absence of free-stream velocity, it is possible to predict the stimulus detected by the canal neuromasts

using a potential flow model (Ćurčić-Blake & van Netten 2006; Goulet *et al.* 2007; Rapo *et al.* 2009). Indeed, the thin boundary layer that develops over the fish does not affect the pressure, as there is no pressure gradient across the thickness of the boundary layer.

All of these studies have been conducted assuming a stationary fish next to a vibrating sphere, when the fish boundary layer is solely due to the vibrating dipole. Several studies have shown that moving fish can also use their lateral line to discriminate stationary objects or arrangements (von Campenhausen *et al.* 1981; Hassan 1986), but little is known about how the viscosity affects the measured signal. In this paper, the fish is assumed to be gliding, resulting in a thicker boundary layer and typically much higher velocities than for a stationary fish. In this configuration, the surface neuromasts may be already saturated and, hence, unable to detect external stimuli, but the canal neuromasts are still able to detect external stimuli (Engelmann *et al.* 2002). Windsor *et al.* (2010*a*,*b*) recently showed that inviscid simulations significantly underestimate the pressure changes along a fish gliding toward or parallel to a wall. Indeed, viscosity causes the fish to displace more water, which can be modelled by adding a stationary displacement thickness. We have shown here that the dynamics of the boundary layer can further enhance the signal measured by the lateral line, as the boundary layer amplifies certain wavelengths and frequencies.

In conclusion, depending on the specific problem studied, the boundary layer can either act as a filter or an amplifier.

4.2. *Lateral line stimulus and effect of swimming speed*

In order to assess the effect of the fish gliding speed we consider specific examples. We start with a fish of length $L = 10$ cm gliding at two body lengths per second, with a Reynolds number $Re = 20\,000$. A large portion of its boundary layer will be convectively unstable with the most unstable wavelength equal to 17 mm (figure 7*f*), corresponding to a frequency around 5 Hz. If the same fish glides at 0.8 body lengths per second, with a Reynolds number $Re = 6250$, the most unstable wavelength is 27 mm (figure 7*e*), with a frequency of 1.5 Hz.

We estimate next the magnitude of the stimulus caused by a nearby cylinder. Figure 13 shows the magnitude of the pressure coefficient changes due to a cylinder as a function of its radius r and distance d. The upper threshold in the detectable distance depends on the background noise, so the isocontour lines represent detectability limits for various noise levels. As expected, a cylinder is more likely to be detected the larger its radius is and the closer it gets. Figure 13(*a–c*) shows that according to the potential flow model, the signal from a given cylinder is slightly stronger at lower Reynolds number due to a thicker boundary layer, but the increase in detectability from $Re = 20\,000$ to $Re = 2000$ is no more than 30 %.

For Reynolds numbers $Re = 2000$ and $Re = 6250$, the amplitude predicted by the potential flow model is in good agreement with the viscous simulations, also within 30 %. Indeed, despite qualitative differences between the pressure signal predicted by the two methods, the amplification factor for these Reynolds numbers is less than one, as shown in figure 11, so the boundary layer does not increase the amplitude of the pressure signal.

However, at $Re = 20\,000$, we have estimated amplification factors greater than two for wavelengths between 0.1 and 0.2. As a result, the amplitude of the viscous pressure signal can be much larger than what would be predicted within an inviscid fluid. If, for example, we assume that pressure coefficient changes larger than 0.4 can be detected, without the effects of the pressure amplification by the boundary

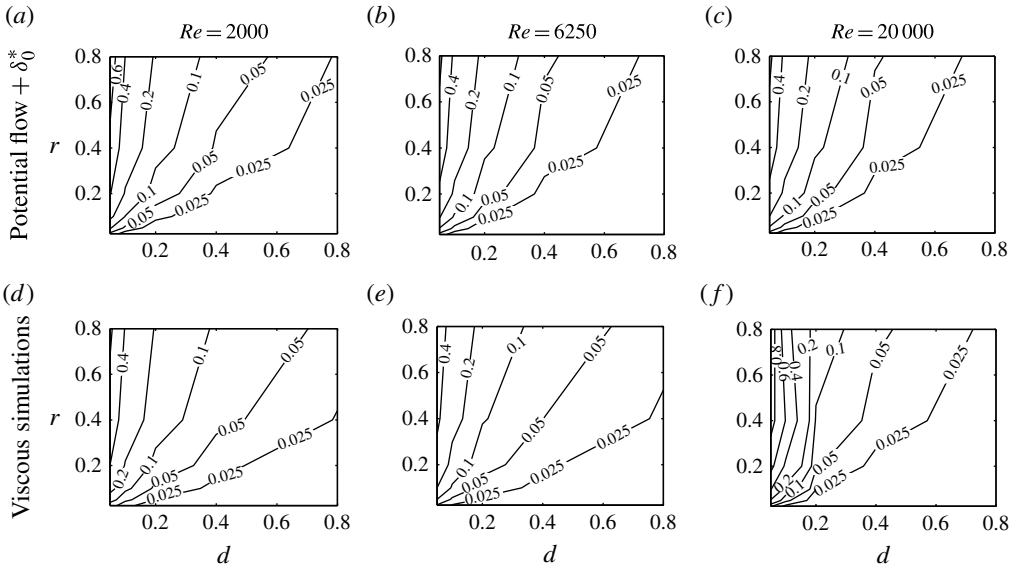

FIGURE 13. Magnitude of the pressure coefficient changes (max $|C_{p'}|$) estimated from potential flow (*a–c*) and viscous simulations (*d–f*).

layer, a cylinder of radius $r = 0.3$ could only be detected at a distance less than 0.06. Because of the amplification, however, it can be detected from twice as far.

It is important to note that since only two-dimensional flows are considered in this paper, pressure changes are overestimated compared with a three-dimensional case. However, the same methodology can be applied to three-dimensional flow, and the results qualitatively transfer to three dimensions. Moreover, comparison between two- and three-dimensional viscous and inviscid simulations of a fish approaching a wall suggest that viscosity impacts the magnitude of the pressure changes more importantly than three-dimensionality (McHenry & Liao 2014).

4.3. *Can the boundary layer facilitate object identification?*

As we have shown, the boundary layer acts as a pressure signal amplifier in the posterior part of the foil, whereas in an inviscid fluid a cylinder would cause significant pressure changes only along the anterior half of the foil. Since both the anterior and posterior parts of the foil are subject to large pressure variations, object detection becomes easier in a viscous rather than in an inviscid fluid. An important question is whether viscous effects can also help with shape identification.

Figure 7 shows that the boundary layer amplifier has a large bandwidth. The bandwidth, defined as the range of wavenumbers for which the amplification is at least $1/\sqrt{2}$ of the maximum amplification, is indeed around 20 for both $Re = 6250$ and $Re = 20\,000$. Therefore, the frequency content of the original signal is largely preserved in the pressure signal after amplification, preserving information concerning the size, distance and shape of the cylinder.

For example, figure 14 shows the difference between the pressure coefficient along a NACA0012 foil passing near the cylinder $\mathscr{C}_1$, with $r = 0.1$, $d = 0.1$, and a slightly larger cylinder, placed further away, cylinder $\mathscr{C}_2$, with $r = 0.125$, $d = 0.12$, both at Reynolds number $Re = 6250$. Stimulus differences estimated by potential flow

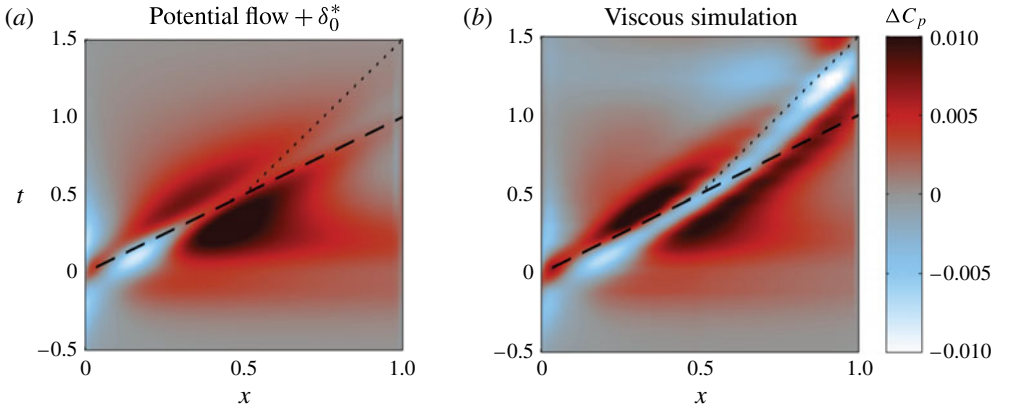

FIGURE 14. (Colour online) Difference between the pressure coefficient changes due to two cylinders: (i) $\mathscr{C}_1$, $C_p(r = 0.1, d = 0.1)$ and (ii) $\mathscr{C}_2$, $C_p(r = 0.125, d = 0.12)$ using potential flow predictions (*a*) and viscous simulations (*b*), both at $Re = 6250$.

(figure 14*a*) and by viscous simulations (figure 14*b*) are provided. Both estimates agree that the magnitude of the stimulus due to $\mathscr{C}_1$ is larger, as indicated by the positive difference at $(x = 0, t = 0)$ followed by a negative difference around $(x = 0.15, t = 0.1)$, corresponding to the positive and negative peaks of the stimulus as seen in figure 6, respectively. The peaks associated with $\mathscr{C}_2$ are also wider, as evidenced by the negative difference on either side of the positive difference, and vice versa. Along the rear half of the foil, however, the inviscid difference is much weaker and has a much lower frequency than the viscous one. In the viscous simulation, the information that the stimulus is stronger but narrower is amplified by the boundary layer, and hence a negative difference, surrounded with positive difference, is seen moving along the posterior half of the foil at half the free-stream velocity. This demonstrates that the boundary layer, in addition to amplifying the pressure signal due to a cylinder, also amplifies the difference between signals caused by two different cylinders, therefore facilitating object identification.

This difference in the amplified disturbance due to different cylinders is even stronger at higher Reynolds number, $Re = 20\,000$, where the amplification is larger. Figure 15(*a–c*) shows disturbances due to three different cylinders, with radius $r = 0.10$, 0.25 and 0.50; and placed at distances $d = 0.06$, 0.10 and 0.12, respectively. All three figures contain a characteristic clockwise vortex, corresponding to a pressure coefficient drop of approximately 0.25. The typical width of this main vortex increases from approximately 0.07 on figure 15(*a*), to 0.1 in figure 15(*b*), to 0.12 in figure 15(*c*). Whereas the small wavelength of the clockwise vortex in figure 15(*a*) leaves room for a counter-clockwise vortex of comparable strength, this second vortex is much weaker in figure 15(*b*), and hardly exists in figure 15(*c*). It appears clearly from these three figures that the wavelength of the amplified disturbance increases with the distance and radius of the cylinder. The difference in the frequency content of the disturbance caused by different objects, as convected by the unstable boundary layer, can clearly be used to distinguish between the objects.

5. Conclusion

The inspiration for this study derives from the reported function of the fish canal neuromasts for detecting pressure gradients. The model problem used in the study, that

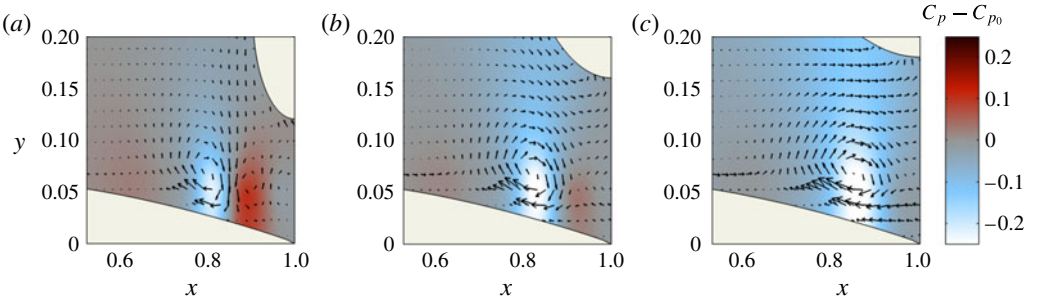

FIGURE 15. (Colour online) Snapshots at $t = 1$ showing the velocity field and pressure coefficient disturbances as a NACA0012 foil passes near three different cylinders with radius r at a distance d: (*a*) $d = 0.06$, $r = 0.10$; (*b*) $d = 0.10$, $r = 0.25$; (*c*) $d = 0.12$, $r = 0.50$; all at $Re = 20\,000$.

of a rigid two-dimensional foil moving at a steady speed near a stationary cylinder, is intended to represent a gliding fish mapping a stationary object, as observed by von Campenhausen *et al.* (1981).

In an inviscid formulation, potential flow can predict accurately the pressure induced by the object on the foil and hence continuous pressure measurements at a finite number of locations can yield the shape of the object (Hassan 1985; Fernandez *et al.* 2011). The experiments we conducted, however, show that potential flow predictions are accurate only over the front half of the body and deviate substantially over the posterior half, with large pressure oscillations present, as shown in figure 3. Hence, potential flow predictions, although easy to obtain even in real time, cannot be used. Whereas under certain conditions the pressure along the body of the fish is not influenced by the viscosity (Rapo *et al.* 2009), when moving in the proximity of objects, it is affected by the viscous interaction between the body and the surrounding flow. When moving toward or gliding parallel to a wall, the inviscid assumption predicts the correct shape of the pressure changes but underestimates them (Windsor *et al.* 2010*a*,*b*). We show that for objects of general shape, dynamic interactions between the boundary layer and the object generate flow and pressure features that do not exist in an inviscid fluid. While there is no pressure gradient across the thickness of the boundary layer, the velocity profile selectively amplifies unsteady perturbations in the form of large vortices travelling at half the free-stream velocity, creating large unsteady pressure variations.

Linear stability analysis of the average boundary layer profile in open water, i.e. in the absence of any nearby obstacle, shows that the large pressure fluctuations in the boundary layer consist of the pressure disturbances induced by the object, amplified through a convective instability of the flow; hence, they are predictable. A methodology is established whereby the potential flow predictions are used to drive an amplification function derived through stability analysis. Without significant additional computations, the resulting model adds to the potential flow pressure prediction a Reynolds number dependent component caused by the passing cylinder, featuring memory and amplification effects. The predictions agree with viscous simulation results, reducing the error by a factor of two compared to the potential flow model, even when the latter includes the steady displacement thickness. Such a model can dramatically improve the performance of existing object identification algorithms (Fernandez *et al.* 2011) and the ability of underwater vehicles to identify objects by measuring pressure fluctuations.

The unsteady pressure fluctuations predicted by linear stability analysis can enhance detectability of the object only if they are combined with potential flow results, because one must know the features of the signal that is being amplified. Therefore, the devised methodology places importance on both the potential flow and the linear instability results. While the features of the pressure induced by a stationary object within the potential flow theory are rather simple and intuitive, the features of the selectively amplified disturbances in the boundary layer are not, and hence would require animal learning in order to be used for detection. There are, indeed, examples of animals training themselves to perform complex tasks, such as trout holding place in the vortical wake of bluff cylinders in steady flow (Liao *et al.* 2003). Given the simple decomposition of the pressure signal we show in this paper, it is plausible that live fish could employ such self-training to detect and map nearby objects.

Acknowledgements

The authors wish to acknowledge support from the Singapore–MIT Alliance for Research and Technology through the CENSAM Program, and from the MIT Sea Grant Program. The authors are also grateful to the Link Foundation for their support through the Link Ocean Engineering & Instrumentation PhD Fellowship awarded to A.P.M.

Appendix A. Boundary data immersed method

In BDIM, the prescribed body kinematics and Navier–Stokes equations are integrated over the fluid and body domains (respectively Ω_f and Ω_b) and convolved with a kernel of radius $\epsilon = 2\Delta x$, where Δx is the finest grid spacing of the mesh. This has the effect of blending the equations smoothly over the fluid/body interface. The kernel used is

$$K_\epsilon(x) = \begin{cases} (1+\cos(|x|\pi/\epsilon))/(2\epsilon) & \text{if } |x| < \epsilon \\ 0 & \text{if } |x| \geqslant \epsilon \end{cases} \tag{A 1}$$

and we call respectively μ_0^ϵ and μ_1^ϵ its zeroth and first central moments (see Maertens & Weymouth 2014 for details).

The BDIM equations for the smoothed velocity field $\boldsymbol{u_\epsilon}$ are valid over the complete domain $\Omega = \Omega_f \cup \Omega_b$ and enforce the no-slip boundary condition at the interface. These equations, integrated over a time-step Δt, are

$$\boldsymbol{u_\epsilon}(t+\Delta t) = \boldsymbol{v}(t+\Delta t) + \left(\mu_0^\epsilon(d) + \mu_1^\epsilon(d)\frac{\partial}{\partial n}\right)(\boldsymbol{u_\epsilon}(t) - \boldsymbol{v}(t+\Delta t) + \boldsymbol{R_{\Delta t}} - \boldsymbol{\partial P_{\Delta t}}) \tag{A 2}$$

$$\nabla \cdot \boldsymbol{u_\epsilon}(t+\Delta t) = 0 \tag{A 3}$$

where $\boldsymbol{v}$ is the velocity field associated with the closest body, $\boldsymbol{n}$ the unitary normal to the closest fluid/solid boundary (pointing toward the fluid), and d the signed distance to the closest boundary ($d > 0$ within the fluid, $d < 0$ inside a body). $\boldsymbol{\partial P_{\Delta t}}$ is the pressure impulse over Δt and $\boldsymbol{R_{\Delta t}}$ accounts for all of the non-pressure terms:

$$\boldsymbol{\partial P_{\Delta t}} = \int_t^{t+\Delta t} \nabla p \, \mathrm{d}\tau \tag{A 4}$$

$$\boldsymbol{R_{\Delta t}} = \int_t^{t+\Delta t} \left[-(\boldsymbol{u_\epsilon} \cdot \nabla)\boldsymbol{u_\epsilon} + \frac{1}{Re_u}\nabla^2 \boldsymbol{u_\epsilon} \right] \mathrm{d}\tau. \tag{A 5}$$

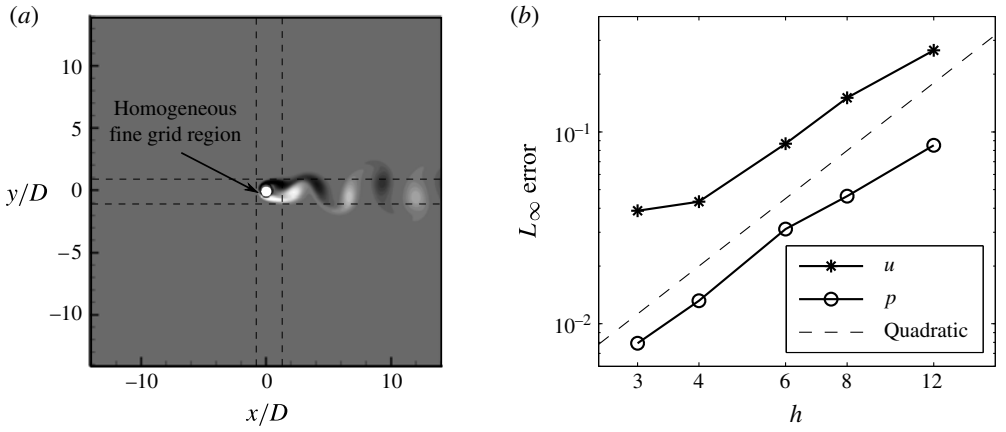

FIGURE 16. Flow past a stationary cylinder at $Re = 100$ with grid size $\Delta x/D = 1/120$. (*a*) Instantaneous vorticity field in the whole computational domain. Dashed lines show where the grid expansion starts. (*b*) L_∞ norm of the velocity and pressure error versus grid size. The grid spacing is $\Delta x/D = h/120$.

Equation (A 2) have been implemented in a Cartesian grid implicit large eddy simulation (ILES) code using an Euler explicit integration scheme with Heun's corrector. They are posed on a staggered Cartesian mesh and central differences are used for all spacial derivatives except in the convective term which uses a flux-limited QUICK scheme for stability.

The canonical case of two-dimensional flow past a static cylinder at Reynolds number $Re = 100$, illustrated in figure 16(*a*), is first considered in order to assess the numerical properties of the proposed method. The flow is simulated in a 28×28 diameter D domain, constant velocity $\boldsymbol{u} = \boldsymbol{U}$ on the inlet, upper and lower boundaries, and a zero gradient exit condition with global flux correction. The grid size is parametrized by parameter h such that the spacing is $\Delta x/D = h/120$ near the cylinder and uses a 1 % geometric expansion ratio for the spacing in the far-field. Since an exact solution for this flow does not exist, we use the solution computed on a highly resolved grid ($h = 1$) as a baseline for computing the error. The same flow is then computed for $h = [3, 4, 6, 8, 12]$, and the velocity and pressure errors are shown on log–log plots in figure 16(*b*), together with a dashed line denoting quadratic convergence.

Next BDIM is applied to a more challenging high-Reynolds-number streamlined-body case relevant to the present work. The two-dimensional flow past a stationary SD7003 aerofoil at 4° angle of attack is computed in a 15×20 chord lengths domain, as illustrated in figure 17. Constant velocity $\boldsymbol{u} = \boldsymbol{U}$ on the inlet, upper and lower boundaries, and a zero gradient exit condition with global flux correction are used. The grid spacing is set to 200 points per chord length L near the aerofoil (corresponding to 16 points across the thickness of the aerofoil) with a 1 % geometric expansion ratio for the grid spacing in the far-field. Figure 18(*a*) shows the average pressure coefficient C_p along the aerofoil and compares it with the body-fitted simulation from Castonguay, Liang & Jameson (2010). Since calculation of the skin friction is carried out ϵ away from the boundary, it is accurate only if the viscous sublayer is thicker than ϵ, which is not the case in the simulations above. In order to accurately calculate the skin friction coefficient C_f and separation point for

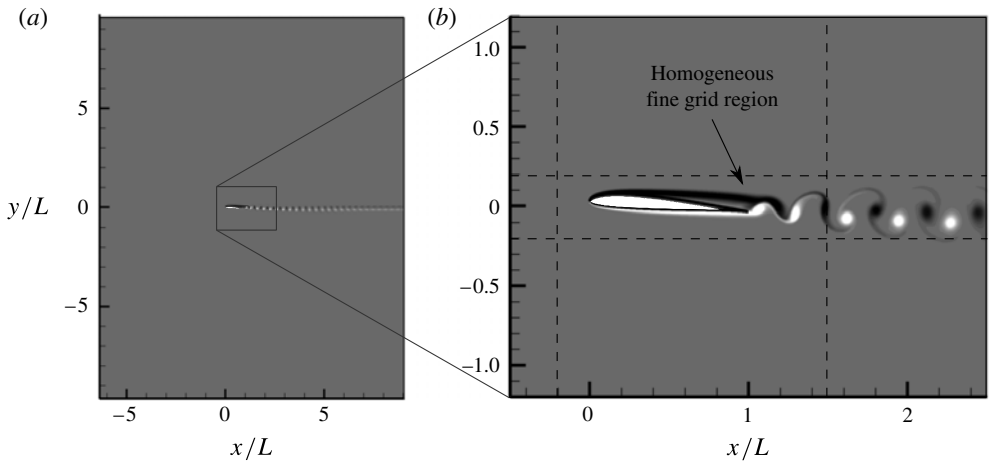

FIGURE 17. Flow past a stationary SD7003 aerofoil at 4° angle of attack and $Re = 10\,000$ with grid size $\mathrm{d}x/L = 1/200$. Instantaneous vorticity field. (*a*) Whole computational domain. (*b*) Zoomed in around the aerofoil. Dashed lines show where the grid expansion starts.

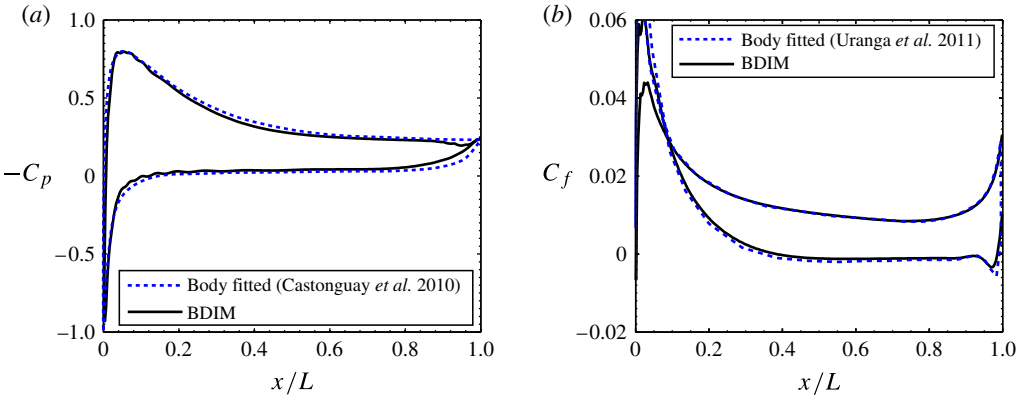

FIGURE 18. (Colour online) Average pressure (*a*) and skin friction (*b*) coefficients around a SD7003 aerofoil at 4° angle of attack and $Re = 10\,000$ with grid size $\Delta x/L = 1/200$. For (*b*), $\Delta y = \Delta x/4$.

this stationary, low angle of attack aerofoil, a finer grid in the cross-flow direction is needed. Here, we increased the density in the y direction by a factor of four. Correcting for the fact that $\boldsymbol{u}_\epsilon(0) = \mu_1^\epsilon \partial \boldsymbol{u}_\epsilon / \partial n$, we calculated the skin friction as

$$C_f(\boldsymbol{x}) = \frac{2\nu}{U^2} \frac{\boldsymbol{u}_\epsilon(\boldsymbol{x} + \epsilon \boldsymbol{n}) \cdot \boldsymbol{n}}{\epsilon + \mu_1^\epsilon(0)}, \tag{A 6}$$

where $\boldsymbol{u}_\epsilon(\boldsymbol{x} + \epsilon \boldsymbol{n})$ is linearly interpolated from the grid. As shown in figure 18(*b*), BDIM predictions compare well with the body-fitted simulations from Uranga *et al.* (2011). We are able to accurately predict the skin friction, the location of separation (around $x/L = 0.38$ versus $x/L = 0.37$ for Uranga *et al.* (2011)) and even the transition

of the boundary layer to turbulent as indicated by the sudden dip in C_f around $x/L = 0.94$.

Appendix B. Varying-coefficient model

Varying-coefficient models form a locally parametric family of structured models that assume the form of the multivariate regression function as

$$g(\boldsymbol{s}, \boldsymbol{z}) = \boldsymbol{z}^t \boldsymbol{a}(\boldsymbol{s}). \tag{B 1}$$

Varying-coefficient models can be seen as a generalization of linear regression in which the coefficients are adjusted locally. By reducing the dimensionality of the functions that need to be identified, structured models are a popular way to avoid the difficulties of large dimensions. If the data to model indeed has the structure of (B 1), then a varying coefficient model can significantly decrease the variance while not increasing the bias, and is therefore expected to fit better than an unstructured model such as (3.7). There are several approaches to estimate $\boldsymbol{a}(\boldsymbol{s})$ in (B 1), among which kernel-local linear regression (Fan & Zhang 1999), which has been selected here for its simplicity.

The model from (B 1) is estimated from a data set consisting of n triplets $(\boldsymbol{s}_j, \boldsymbol{z}_j, y_j)$. The local linear estimator $\hat{\boldsymbol{a}}(\boldsymbol{s})$ is calculated by minimizing:

$$L(\boldsymbol{a}, \boldsymbol{B}) = \sum_{j=1}^{n} [y_j - \boldsymbol{z}_j^t \boldsymbol{a} - \boldsymbol{z}_j^t \boldsymbol{B}(\boldsymbol{s}_j - \boldsymbol{s})]^2 K_h(\|\boldsymbol{s}_j - \boldsymbol{s}\|), \tag{B 2}$$

where $K_h(t) = K(t/h)/h$ with K the unit Gaussian kernel. In the case of (3.6), $\boldsymbol{s}_j = (k_j, t_j)$ with dimensionality $d_s = 2$, $\boldsymbol{z}_j = \tilde{p}_i(k_j, t_j, \mathscr{C}_j)$ with $d_z = 1$, and $y_j = |\tilde{p}(k_j, t_j, \mathscr{C}_j) - \tilde{p}_i(k_j, t_j, \mathscr{C}_j)|$. Here, $\boldsymbol{a}$ is a d_z-vector while $\boldsymbol{B}$ is a $d_z \times d_s$ matrix. The smoothing parameter h is chosen by 10-fold cross-validation.

Let us define

$$\left.\begin{array}{l} \boldsymbol{Z} = [z_1, \ldots, z_n]^t, \quad \boldsymbol{y} = [y_1, \ldots, y_n]^t \\ \boldsymbol{S}_s = [\boldsymbol{s}_1 - \boldsymbol{s}, \ldots, \boldsymbol{s}_n - \boldsymbol{s}], \quad \boldsymbol{w}_s = \mathrm{diag}\left[K_h(\|\boldsymbol{s}_1 - \boldsymbol{s}\|), \ldots, K_h(\|\boldsymbol{s}_n - \boldsymbol{s}\|)\right] \\ \boldsymbol{\Gamma}_s = \left[\boldsymbol{Z}, \mathrm{diag}[\boldsymbol{S}_s(1, :)]\boldsymbol{Z}, \ldots, \mathrm{diag}[\boldsymbol{S}_s(d_s, :)]\boldsymbol{Z}\right]. \end{array}\right\} \tag{B 3}$$

The local linear estimator solution to the optimization problem (B 2) is

$$\hat{\boldsymbol{a}}(\boldsymbol{s}) = \left[\boldsymbol{I}_{d_z}, \boldsymbol{0}_{(d_z, d_s)}\right] \left(\boldsymbol{\Gamma}_s^t \boldsymbol{w}_s \boldsymbol{\Gamma}_s\right)^{-1} \boldsymbol{\Gamma}_s^t \boldsymbol{w}_s, \boldsymbol{y}, \tag{B 4}$$

where $\boldsymbol{I}_{d_z}$ is a size d_z identity matrix and $\boldsymbol{0}_{(d_z, d_s)}$ a size $d_z \times (d_z * d_s)$ matrix with each entry being 0.

The viscous simulations used to estimate $\hat{\boldsymbol{a}}$ consist of cylinders ranging in radius r from 0.025 to 0.8 and in distance d from 0.05 to 0.8. For each cylinder, wavenumbers $k = 2\pi[2, 3, \ldots, 8]$ are used, as well as a number of time steps proportional to the distance between the centre of the cylinder and the foil. Table 3 shows the size and distance of the cylinders used to estimate $\hat{\boldsymbol{a}}$, as well as the number of time step for each cylinder. This represents a total of $363 \times 7 = 2541$ data points, half of which were randomly assigned to the learning set, while the other half was only used for testing and to compute the test error reported in table 2.

r	d				
	0.05	0.1	0.2	0.4	0.8
0.8	5	5	5	4	4
0.4	9	9	7	6	6
0.2	17	14	11	7	—
0.1	27	21	14	9	—
0.05	39	27	17	—	—
0.025	49	33	18	—	—

TABLE 3. Number of time steps used for each cylinder radius r and distance d.

REFERENCES

BERS, A. 1983 Basic plasma physics I. In *Handbook of Plasma Physics* (ed. M. N. Rosenbluth & R. Z. Sagdeev), North-Holland Publishing Company.

VON CAMPENHAUSEN, C., RIESS, I. & WEISSERT, R. 1981 Detection of stationary objects by the blind cave fish *Anoptichthys jordani (Characidae)*. *J. Compar. Physiol.* A **143** (3), 369–374.

CASTONGUAY, P., LIANG, C. & JAMESON, A. 2010 Simulation of transitional flow over airfoils using the spectral difference method. In *40th AIAA Fluid Dynamics Conference, Chicago, IL*, American Institute of Aeronautics and Astronautics.

CHOMAZ, J.-M. 2005 Global instabilities in spatially developing flows: non-normality and nonlinearity. *Annu. Rev. Fluid Mech.* **37**, 357–392.

CHU, W. S., LEE, K. T., SONG, S. H., HAN, M. W., LEE, J. Y., KIM, H. S., KIM, M. S., PARK, Y. J., CHO, K. J. & AHN, S. H. 2012 Review of biomimetic underwater robots using smart actuators. *Intl J. Precis. Engng Manuf.* **13** (7), 1281–1292.

CONSI, T. R., ATEMA, J., GOUDEY, C. A., CHO, J. & CHRYSSOSTOMIDIS, C. 1994 AUV guidance with chemical signals. In *Proceedings of the 1994 Symposium on Autonomous Underwater Vehicle Technology (AUV'94)*, pp. 450–455. IEEE.

COOMBS, S., BLECKMANN, H., FAY, R. & POPPER, A. N. 2014 *The Lateral Line System*. Springer.

COOMBS, S. & BRAUN, C. B. 2003 Information processing by the lateral line system. In *Sensory Processing in Aquatic Environments*, 1st edn (ed. S. P. Collin & N. J. Marshall), pp. 122–138. Springer.

COOMBS, S. & MONTGOMERY, J. C. 1999 The enigmatic lateral line system. In *Comparative Hearing: Fish and Amphibians* (ed. R. Fay & A. N. Popper), pp. 319–362. Springer.

ĆURČIĆ-BLAKE, B. & VAN NETTEN, S. M. 2006 Source location encoding in the fish lateral line canal. *J. Expl Biol.* **209** (8), 1548–1559.

ENGELMANN, J., HANKE, W. & BLECKMANN, H. 2002 Lateral line reception in still-and running water. *J. Compar. Physiol.* A **188** (7), 513–526.

FAN, J. & ZHANG, W. 1999 Statistical estimation in varying coefficient models. *Ann. Stat.* **27** (5), 1491–1518.

FERNANDEZ, V. I., MAERTENS, A., YAUL, F., DAHL, J., LANG, J. & TRIANTAFYLLOU, M. 2011 Lateral-line-inspired sensor arrays for navigation and object identification. *Mar. Technol. Soc. J.* **45** (4), 130–146.

GOULET, J., ENGELMANN, J., CHAGNAUD, B. P., FRANOSCH, J. M., SUTTNER, M. D. & VAN HEMMEN, J. L. 2007 Object localization through the lateral line system of fish: theory and experiment. *J. Compar. Physiol.* A **194** (1), 1–17.

HASSAN, E. S. 1985 Mathematical analysis of the stimulus for the lateral line organ. *Biol. Cybern.* **52** (1), 23–36.

HASSAN, E. S. 1986 On the discrimination of spatial intervals by the blind cave fish (*Anoptichthys jordani*). *J. Compar. Physiol.* A **159** (5), 701–710.

HASTIE, T. & TIBSHIRANI, R. 1993 Varying-coefficient models. *J. R. Stat. Soc.* B **55** (4), 757–796.

HUERRE, P. & MONKEWITZ, P. A. 1990 Local and global instabilities in spatially developing flows. *Annu. Rev. Fluid Mech.* **22** (1), 473–537.

LIAO, J. C., BEAL, D. N., LAUDER, G. V. & TRIANTAFYLLOU, M. S. 2003 Fish exploiting vortices decrease muscle activity. *Science* **302** (5650), 1566–1569.

MACIVER, M. A., FONTAINE, E. & BURDICK, J. W. 2004 Designing future underwater vehicles: principles and mechanisms of the weakly electric fish. *IEEE J. Ocean. Engng* **29** (3), 651–659.

MAERTENS, A. P. & WEYMOUTH, G. D. 2014 Accurate Cartesian-grid simulations of near-body flows at intermediate Reynolds numbers. *Comput. Meth. Appl. Mech. Engng* (in press).

MARQUILLIE, M. & EHRENSTEIN, U. 2003 On the onset of nonlinear oscillations in a separating boundary-layer flow. *J. Fluid Mech.* **490**, 169–188.

MCHENRY, M. J. & LIAO, J. C. 2014 The hydrodynamics of flow stimuli. In *The Lateral Line System*, pp. 73–98. Springer.

MCHENRY, M. J., STROTHER, J. A. & VAN NETTEN, S. M. 2008 Mechanical filtering by the boundary layer and fluid–structure interaction in the superficial neuromast of the fish lateral line system. *J. Compar. Physiol.* A **194** (9), 795–810.

MONTGOMERY, J. C., COOMBS, S. & BAKER, C. F. 2001 The mechanosensory lateral line system of the hypogean form of *Astyanax fasciatus*. *Environ. Biol. Fishes* **62** (1), 87–96.

VAN NETTEN, S. M. 2006 Hydrodynamic detection by cupulae in a lateral line canal: functional relations between physics and physiology. *Biol. Cybern.* **94** (1), 67–85.

OERTEL, H. 1990 Wakes behind blunt bodies. *Annu. Rev. Fluid Mech.* **22** (1), 539–562.

ORSZAG, S. A. 1971 Accurate solution of the Orr–Sommerfeld stability equation. *J. Fluid Mech.* **50** (4), 689–703.

RAPO, M. A., JIANG, H., GROSENBAUGH, M. A. & COOMBS, S. 2009 Using computational fluid dynamics to calculate the stimulus to the lateral line of a fish in still water. *J. Expl Biol.* **212** (10), 1494–1505.

REED, H. L., SARIC, W. S. & ARNAL, D. 1996 Linear stability theory applied to boundary layers. *Annu. Rev. Fluid Mech.* **28** (1), 389–428.

SALUMÄE, T. & KRUUSMAA, M. 2013 Flow-relative control of an underwater robot. *Proc. R. Soc.* A **469** (2153), 20120671.

TEYKE, T. 1988 Flow field, swimming velocity and boundary layer: parameters which affect the stimulus for the lateral line organ in blind fish. *J. Compar. Physiol.* A **163** (1), 53–61.

THEOFILIS, V. 2011 Global linear instability. *Annu. Rev. Fluid Mech.* **43**, 319–352.

TRIANTAFYLLOU, G. S., TRIANTAFYLLOU, M. S. & CHRYSSOSTOMIDIS, C. 1986 On the formation of vortex streets behind stationary cylinders. *J. Fluid Mech.* **170**, 461–477.

URANGA, A., PERSSON, P.-O., DRELA, M. & PERAIRE, J. 2011 Implicit large eddy simulation of transition to turbulence at low Reynolds numbers using a discontinuous Galerkin method. *Intl J. Numer. Meth. Engng* **87** (1–5), 232–261.

WEBB, J. F. 2000 Mechanosensory lateral line: functional morphology and neuroanatomy. In *Handbook of Experimental Animals: The Laboratory Fish*, pp. 236–244. Academic Press.

WEIDEMAN, J. A. & REDDY, S. C. 2000 A MATLAB differentiation matrix suite. *ACM Trans. Math. Softw.* **26** (4), 465–519.

WEYMOUTH, G. D., DOMMERMUTH, D. G., HENDRICKSON, K. & YUE, D. K.-P. 2006 Advancements in Cartesian-grid methods for computational ship hydrodynamics. In *26th Symposium on Naval Hydrodynamics, Rome, Italy, 17–22 September 2006*, Office of Naval Research.

WEYMOUTH, G. D. & TRIANTAFYLLOU, M. S. 2013 Ultra-fast escape of a deformable jet-propelled body. *J. Fluid Mech.* **721**, 367–385.

WEYMOUTH, G. D. & YUE, D. K.-P. 2011 Boundary data immersion method for Cartesian-grid simulations of fluid–body interaction problems. *J. Comput. Phys.* **230** (16), 6233–6247.

WIBAWA, M. S., STEELE, S. C., DAHL, J. M., RIVAL, D. E., WEYMOUTH, G. D. & TRIANTAFYLLOU, M. S. 2012 Global vorticity shedding for a vanishing wing. *J. Fluid Mech.* **695**, 112–134.

WINDSOR, S. P. & MCHENRY, M. J. 2009 The influence of viscous hydrodynamics on the fish lateral-line system. *Integr. Compar. Biol.* **49** (6), 691–701.

WINDSOR, S. P., NORRIS, S. E., CAMERON, S. M., MALLINSON, G. D. & MONTGOMERY, J. C. 2010*a* The flow fields involved in hydrodynamic imaging by blind Mexican cave fish (*Astyanax fasciatus*). Part I: open water and heading towards a wall. *J. Expl Biol.* **213** (22), 3819–3831.

WINDSOR, S. P., NORRIS, S. E., CAMERON, S. M., MALLINSON, G. D. & MONTGOMERY, J. C. 2010*b* The flow fields involved in hydrodynamic imaging by blind Mexican cave fish (*Astyanax fasciatus*). Part II: gliding parallel to a wall. *J. Expl Biol.* **213** (22), 3832–3842.

WINDSOR, S. P., TAN, D. & MONTGOMERY, J. C. 2008 Swimming kinematics and hydrodynamic imaging in the blind Mexican cave fish (*Astyanax fasciatus*). *J. Expl Biol.* **211** (18), 2950–2959.

WU, X., JACOBS, R. G., HUNT, J. C. R. & DURBIN, P. A. 1999 Simulation of boundary layer transition induced by periodically passing wakes. *J. Fluid Mech.* **398**, 109–153.